A complex network based early warning indicator of the MOC collapse

Master thesis research by
Mirjam van der Mheen

Supervised by
Prof Dr. H.A. Dijkstra
Matthijs den Toom
Werner Kramer

Abstract

Early warning indicators of the collapse of the Atlantic Meridional Overturning Circulation (MOC) have up to now only been based on temporal correlations of single time series. In this thesis, we use spatial correlations of the time series of the temperature and salinity fields to construct complex networks. These networks are constructed at different points approaching the tipping point of the MOC. In these points, we observe a clear evolution of the network degree. We explain this evolution by considering the eigenvectors and the empirical orthogonal functions (EOFs) of the system. To investigate the application of this procedure to grids with limited spatial resolution, we also construct networks from two different limited grids. We find a new early warning indicator for the MOC based on the evolution in the network degree. This indicator is also applicable to the limited grids.

Contents

1 Introduction **7**
1.1 Climate variability . . . 7
1.2 Atlantic Meridional Overturning Circulation . . . 8
1.3 Tipping points and early warning signals . . . 10
1.4 Networks in climate . . . 10
1.5 Scope of this thesis . . . 11

2 Theory **13**
2.1 Meridional overturning circulation (MOC) . . . 13
2.1.1 Stommel two-box model . . . 13
2.1.2 Stommel three-box model . . . 16
2.1.3 Physical mechanisms . . . 19
2.2 Bifurcations . . . 20
2.2.1 Saddle-node bifurcation . . . 20
2.2.2 Pitchfork bifurcation . . . 21

3 Model and Method **23**
3.1 THCM . . . 23
3.2 Network construction . . . 25
3.2.1 Network properties . . . 25

4 Results: Symmetrical forcing **27**
4.1 Bifurcation diagram . . . 27
4.2 Networks . . . 30
4.3 Eigenvectors . . . 33
4.4 Empirical Orthogonal Functions (EOFs) . . . 34
4.4.1 Reconstructed networks . . . 38
4.4.2 Correlation EOFs . . . 41
4.5 Limited grid networks . . . 45
4.6 Warning signal . . . 48

5 Results: Asymmetrical forcing **51**
5.1 Bifurcation diagram . . . 51
5.2 Networks . . . 53
5.3 Empirical Orthogonal Functions (EOFs) . . . 55
5.3.1 Reconstructed Networks . . . 57
5.4 Limited grid networks . . . 59
5.5 Warning signal . . . 62

6 Discussion and Conclusion **63**

A Network tests **65**
A.1 Networks with different thresholds . . . 65
A.2 Networks from longer time series . . . 68

Chapter 1

Introduction

1.1 Climate variability

In our climate system, variability arises due to several different forcing mechanisms and processes. Because of this, climate variability occurs on different time scales, ranging from fluctuations of several hours to climatic transitions of thousands of years (Mitchell (1976)). Figure 1.1 shows an impression that provides an overview of all these different scales. In the figure, a power spectrum of the variance has been constructed using many different time series, obtained from various climatic records.

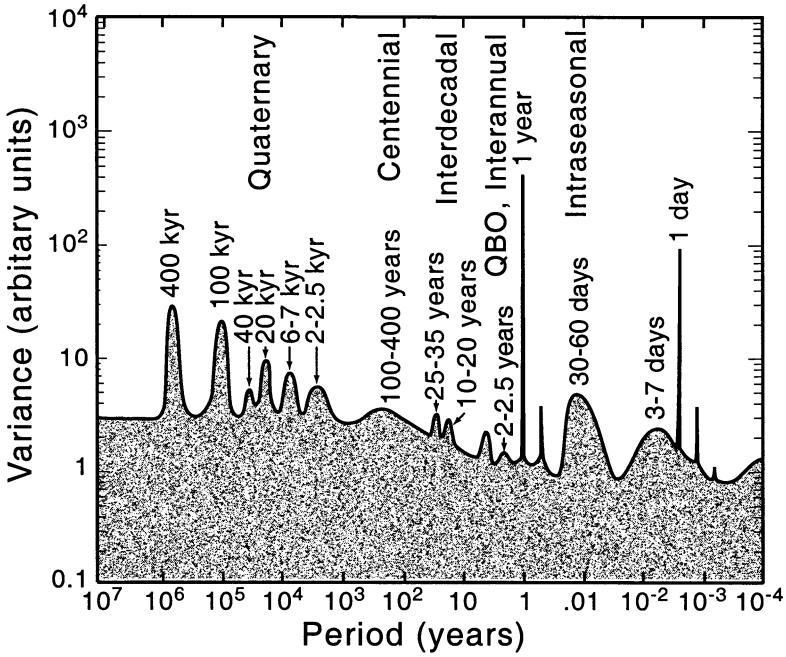

Figure 1.1: An impression of the power spectrum of climate variability showing the amount of variance in each frequency range. Figure from Dijkstra and Ghil (2005), figure first produced by Mitchell (1976).

Figure 1.1 shows familiar variability on the shorter time scales. For example, daily fluctuations can be seen as a sharp peak at 1 day and at 3-7 days the variability of midlatitude weather systems is present. Intraseasonal variability occurs at 30-60 days and interseasonal fluctuations are seen yearly. At slightly longer time scales interannual variability occurs. The El Niño phenomenon is an important aspect of these year-to-year variations, occurring roughly every four years for a period of about one year. In the left of figure 1.1, paleoclimatic variability is present at much longer time scales. In the last two million years during the Quaternary, glaciation cycles are prominent. Within these glaciation cycles higher frequency oscillations are also present. The Dansgaard-Oeschger cycle, at a time scale of 1-2.5 kyr is one of these (Dansgaard et al. (1993)). During a Dansgaard-Oeschger event, rapid temperature changes occur. Figure 1.2 shows the δ^{18}O record (which is a proxy for air temperature) from an ice core in Greenland of the

past 120 thousand years, with the Dansgaard-Oeschger events indicated by numbers.

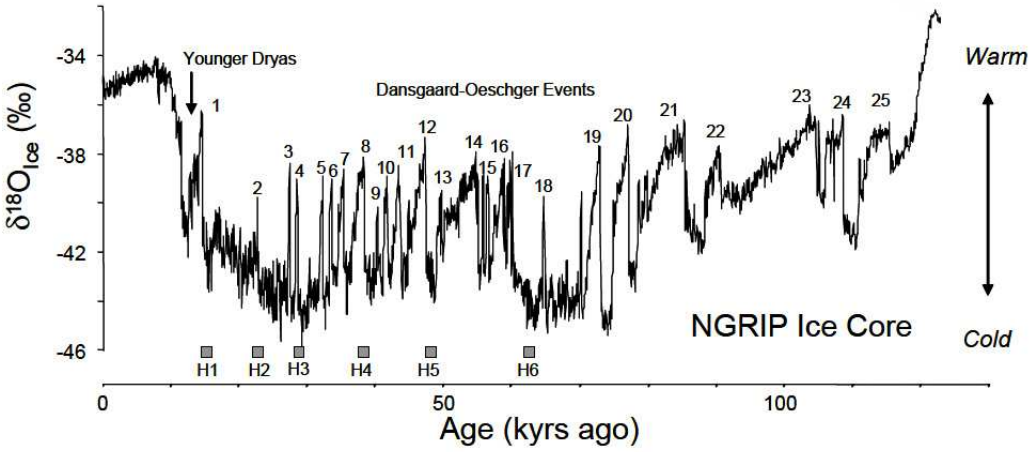

Figure 1.2: The δ^{18}O record from an ice core from the North Greenland Ice Core Project. The Dansgaard-Oeschger events are numbered. Figure from Clement and Peterson (2008).

Variations in the ocean circulation play a key role in climate variability and climate change (Dijkstra and Ghil (2005)). Since the oceans are important for meridional heat transport, changes in the circulation can affect the distribution of temperature and precipitation significantly (Vellinga and Wood (2002)). It is suspected that large-scale transitions of the ocean circulation are responsible for the climate change during the Dansgaard-Oeschger events. An important transition of the circulation is the reversal of the Atlantic Meridional Overturning Circulation (MOC).

1.2 Atlantic Meridional Overturning Circulation

An impression of the wind-driven surface ocean currents in the Atlantic Ocean is shown in figure 1.3. The Gulf Stream is a warm current that flows northward along the west side of the Atlantic basin. With a volume transport of up to 88 Sverdrup (1 Sv = 10^6 m^{3}s^{-1}), this is a strong current. For the most part, the northward volume transport is compensated in the subtropical gyre. However, part of the Gulf Stream continues poleward as the North Atlantic Drift. This is a slow current that transports warm water to the north and contributes to the relatively mild European climate. On its way northward, the relatively warm and saline water of the North Atlantic Drift is cooled. In the Greenland Sea and the Labrador Sea the water column becomes unstably stratified and convection occurs. In this way, North Atlantic Deep Water is formed. This water is transported southwards as a deep current. Over the entire Atlantic, upwelling occurs to compensate for the northern sinking.

The total system of a meridional surface current, sinking, a compensating deep current and upwelling is referred to as the Meridional Overturning Circulation. During the Dansgaard-Oeschger events it is thought that a rapid reduction in strength or even reversal of the MOC occurred (Bond et al. (1993), Rhamstorf (1995), Knutti et al. (2004)). Such an abrupt change is referred to as a tipping point. The MOC can reach a tipping point when the freshwater forcing in the northern North Atlantic is changed. This tipping point is associated with a saddle-node bifurcation, which we shall consider in more detail in chapter 2.

Due to anthropogenic greenhouse forcing the high-latitude temperature and precipitation is expected to increase (Meehl et al. (2007)). A further input of freshwater into the system is expected due to the melting of the Greenland Ice Cap. All of these effects decrease the density of the polar surface waters and therefore the stability of the stratification increases and convective processes are inhibited. As a consequence, the Atlantic MOC is influenced by anthropogenic warming (Gregory et al. (2005)). Since changes in the MOC affect the whole climate system (Vellinga and Wood (2002), Meehl et al. (2007)), it is important to have a good understanding of this dynamical system and its potential tipping points. Ideally, we would like to find an indicator that provides an early warning signal for the transition in the Meridional Overturning Circulation.

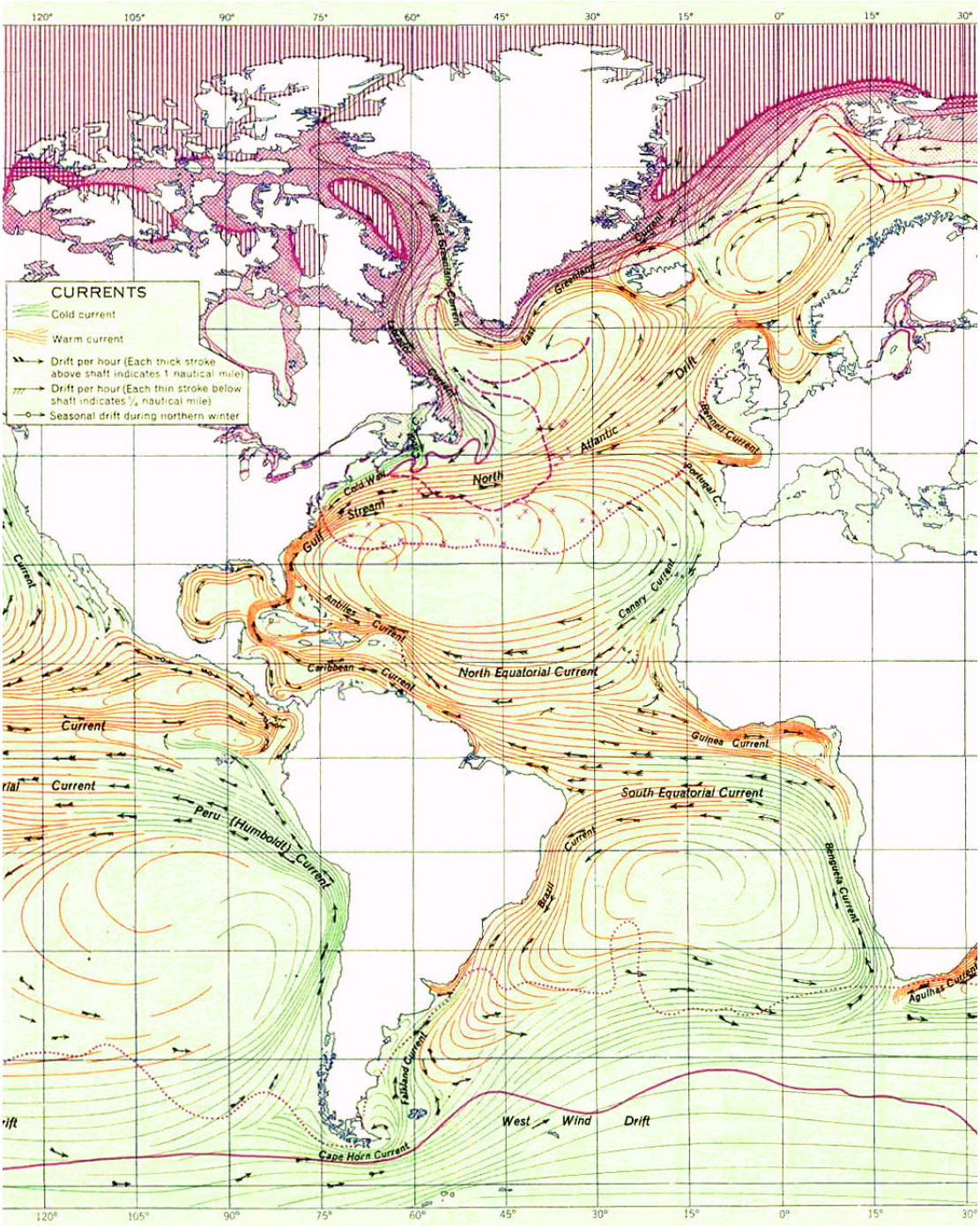

Figure 1.3: Wind-driven surface ocean currents in the Atlantic Ocean. Figure from Army Service Forces Manual M-101 (1943).

1.3 Tipping points and early warning signals

The sensitivity of the Atlantic Meridional Overturning Circulation with respect to freshwater fluxes in the northern North Atlantic has been studied extensively using Ocean General Circulation Models (OGCMs). The issue whether the MOC could collapse into a state where no North Atlantic Deep Water is formed, and instead only southern sources of deep water are active, has been of specific interest (Bryan (1986), Maier-Reimer and Mikolajewicz (1989)). This has given rise to the so-called hosing experiment, which is a procedure where an anomalous freshwater flux is gradually applied over a broad swath in the subpolar North Atlantic until the overturning cell collapses (Rhamstorf (1995), et al. (2006)). We will further explain this procedure in chapter 3 and it will also be applied in chapter 5. A diversity of models has shown that this transition in the MOC can occur due to the presence of a saddle-node bifurcation (Dijkstra (2005)).

In recent years, there has been an increasing interest to develop early warning indicators for the proximity of saddle-node bifurcation points in so-called slow/fast systems (Kuehn (2011)). As in the case with the hosing experiment, in these systems a parameter is slowly varied in time until the tipping point is approached. For the Meridional Overturning Circulation, these early warning indicators are based on temporal characteristics such as the slowdown (enhanced autocorrelation) and enhanced variance of the system's behavior when approaching the tipping point. The techniques that are currently used, such as degenerate fingerprinting (Held and Kleinen (2004)), degenerate fluctuation analysis (Lenton and Schnellnhuber (2007)) and potential analysis (Livina et al. (2010)) all require very long time series to be able to detect the proximity of the saddle-node bifurcation. By using complex network theory, we want to find a new early warning indicator that is based on spatial rather than temporal correlations.

1.4 Networks in climate

The use of network theory has brought new insights in climate science as well as in other fields. For example, (virtual) social networks as well as traffic flow can be studied by using networks (Cho (2009)). Epidemiology has also benefitted from graph theory (Stanley and Havlin (2003)).

A network consists of nodes that are connected by links. The nodes can be virtually anything. In social networks the nodes are people and the links between them are social ties or interactions. When studying the climate system, the nodes are generally grid points of certain climate variables, such as temperature or salinity. The nodes can be seen as oscillators corresponding to the time series of a variable. The network then consists of interacting oscillators, where the interactions are determined by correlations (Steinhaeuser et al. (2010)).

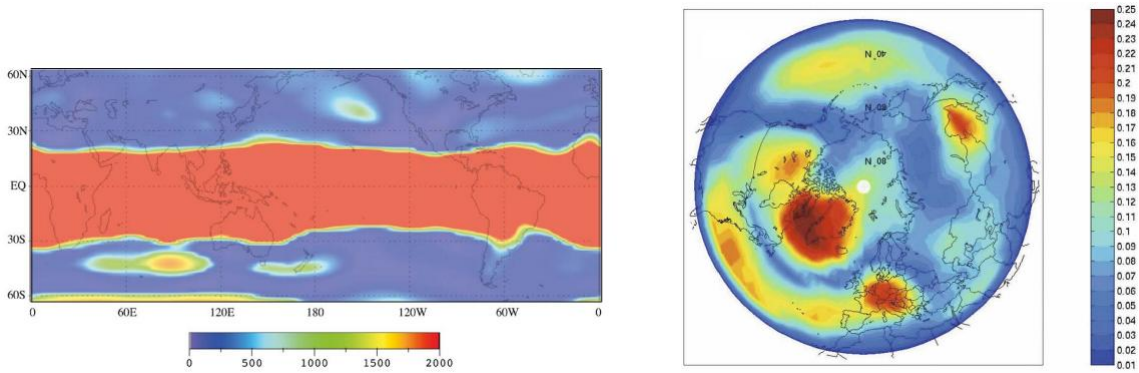

(a) (b)

Figure 1.4: (a) Number of total links in the climate network at each geographic location, constructed from the surface air temperature. Figure from Tsonis and Roebber (2004). (b) Total number of links for the extratropical network from 30°N to 90°N. Figure from Tsonis et al. (2008).

Though the use of network theory in climate science is relatively new, several interesting results have already been obtained. When constructing a global network from the surface air temperature, Tsonis and Roebber (2004) found that in general the nodes in the tropics have a lot more links than nodes at higher latitudes, see figure 1.4a. At higher latitudes some regions with high connectivity are observed. Tsonis

et al. (2008) show that these regions are associated with atmospheric teleconnections. For example, when Tsonis et al. (2008) constructed a network with only nodes north of 30°N, the North Atlantic Oscillation (NAO) pattern shows up (figure 1.4b).

Specific phenomena have also been studied using networks. Yamasaki et al. (2008) find that during an El Niño event, the number of links in the global surface temperature network decrease significantly. This is seemingly in contradiction with the known impact of El Niño on the global climate system. By using directed links, Gozolchiani and Havlin (2010) found that the number of links going into the El Niño basin decreases but the number of outgoing links increases. Therefore, it can be concluded that the equatorial Pacific becomes autonomous during El Niño events. It was also observed that the amount of links directed into the basin increases just before the occurrence of an event. This result suggests that it might be possible to predict an El Niño event by using network analysis and opens the possibility of predicting other climate events.

1.5 Scope of this thesis

In this work, we use a two-dimensional cross-section model of the Atlantic Ocean where only the density-driven MOC is represented. We then construct networks from the temperature and salinity at different points along the bifurcation diagram of the Meridional Overturning Circulation. By investigating the evolution of the network topology, we hope to find a useful indicator that provides a warning signal of the approaching tipping point.

In chapter 2 we provide some background theory of the MOC and bifurcations, chapter 3 considers the model and methods we use and results are presented in chapters 4 and 5. In these chapters we also discuss possible indicators for a warning signal. Our conclusions are given in chapter 6.

Chapter 2

Theory

We consider some MOC transition theory using the Stommel two-box and three-box models in section 2.1. Based on these box models, we see that bifurcations arise and therefore discuss fixed points and several types of bifurcations in section 2.2.

2.1 Meridional overturning circulation (MOC)

The ocean circulation is mainly driven by momentum fluxes from the wind and by heat and freshwater fluxes at the ocean-atmosphere interface. The fluxes of heat and freshwater result in a large-scale density driven circulation. This circulation manifests itself in the meridional-depth plane and is therefore called the Meridional Overturning Circulation (MOC), also referred to as the thermohaline circulation.

At low latitudes there is heat input into the system while at higher latitudes there is heat loss. This meridional temperature gradient results in a density driven surface flow directed from the equator towards the poles, due to sinking of denser cold water at the poles. On the other hand, there is substantial evaporation at low latitudes, which increases the salinity and therefore the density. This leads to sinking near the equator and results in an equator-ward surface flow. From this it is obvious that the surface heat flux and the freshwater flux have opposing effects. The Stommel two- and three-box models provide insights as to what happens when the Meridional Overturning Circulation is driven by both fluxes.

2.1.1 Stommel two-box model

The Stommel two-box model consists of an equatorial and a polar box and was first introduced by Stommel (1961). At the surface, both boxes are connected by an overflow region and at the bottom by a capillary tube. The volume of the equatorial box is V_e and of the polar box V_p. Both boxes contain well mixed water with temperatures T_e and T_p and salinities S_e and S_p, where the subscript e means equatorial and p polar. The two-box model is sketched in figure 2.1.
The surface flow rate is given by Ψ_* and is linearly related to the density difference between the two boxes

$$\Psi_* = \lambda \frac{\rho_{p*} - \rho_{e*}}{\rho_0}.$$

Here, the subscript $*$ indicates dimensional quantities, λ is a hydraulic constant and ρ_0 a reference density. From this equation it follows that the flow rate Ψ_* is positive if the water is heavier in the polar box, so if the flow is directed from the equator toward the pole. The densities ρ_e and ρ_p are found by using a linear equation of state,

$$\rho_* = \rho_0(1 - \alpha_T(T_* - T_0) + \alpha_S(S_* - S_0)),$$

where T_0 and S_0 are a reference temperature and salinity, respectively. The quantities α_T and α_S are the thermal expansion and haline contraction coefficients.

The circulation in the box model is driven by a density gradient, which is caused by the exchange of heat and salt at the surface. The exchange at the ocean-atmosphere interface is modelled through a relaxation to a prescribed surface temperature T^a and salinity S^a. The relaxation coefficients for temperature and salinity are given by C^T and C^S and they differ for each box. The heat and salt

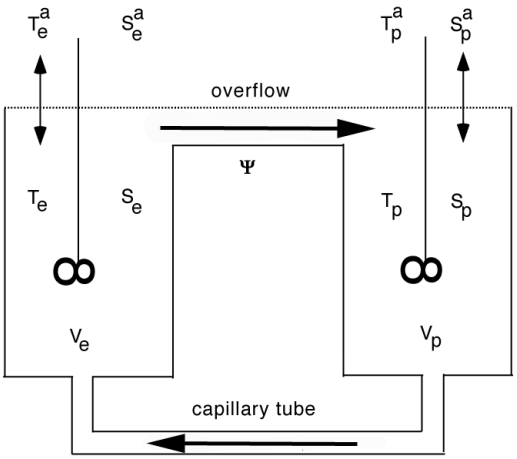

Figure 2.1: Sketch of the Stommel two-box model. An equatorial and a polar reservoir contain well mixed water and are connected by a surface overflow region and a capillary tube at the bottom. The circulation is driven by density gradients between the water in both boxes. The density gradient is caused by exchange of heat and freshwater at the ocean-atmosphere interface. Figure from Dijkstra (2005).

balances in the equatorial and polar box are then given by

$$V_e \frac{dT_{e*}}{dt_*} = C_e^T (T_e^a - T_{e*}) + |\Psi_*|(T_{p*} - T_{e*}), \tag{2.1a}$$

$$V_p \frac{dT_{p*}}{dt_*} = C_p^T (T_p^a - T_{p*}) + |\Psi_*|(T_{e*} - T_{p*}), \tag{2.1b}$$

$$V_e \frac{dS_{p*}}{dt_*} = C_e^S (S_e^a - S_{e*}) + |\Psi_*|(S_{p*} - S_{e*}), \tag{2.1c}$$

$$V_p \frac{dS_{p*}}{dt_*} = C_p^S (S_p^a - S_{p*}) + |\Psi_*|(S_{e*} - S_{p*}). \tag{2.1d}$$

For simplicity, we assume that $\frac{C_e^T}{V_e} = \frac{C_p^T}{V_p} \equiv R_T$ and $\frac{C_e^S}{V_e} = \frac{C_p^S}{V_p} \equiv R_S$. By scaling time, temperature, salinity and flow rate with $\frac{1}{R_T}$, $\frac{V_e V_p R_T}{\lambda \alpha_T (V_e + V_p)}$, $\frac{V_e V_p R_T}{\lambda \alpha_S (V_e + V_p)}$ and $\frac{V_e V_p R_T}{V_e + V_p}$ respectively, we find the dimensionless equivalent of equations 2.1

$$\frac{dT}{dt} = \eta_1 - T(1 + |T - S|), \tag{2.2a}$$

$$\frac{dS}{dt} = \eta_2 - S(\eta_3 |T - S|), \tag{2.2b}$$

where the subscript $*$ has been removed to indicate dimensionless quantities. Furthermore, $T = T_e - T_p$, $S = S_e - S_p$ and the dimensionless flow rate is given by $\Psi = T - S$. The three parameters η_1, η_2 and η_3 are given by

$$\eta_1 = \frac{(T_e^a - T_p^a)\lambda \alpha_T (V_e + V_p)}{V_e V_p R_T},$$

$$\eta_2 = \frac{R_S}{R_T} \frac{(S_e^a - S_p^a)\lambda \alpha_S (V_e + V_p)}{V_e V_p R_T},$$

$$\eta_3 = \frac{R_S}{R_T}.$$

Here, η_1 is a measure of the thermal forcing; η_2 a measure of the saline forcing or, alternatively, a freshwater parameter; η_3 a ratio of adjustment time scales to heat and salt perturbations at the surface. We are interested in the freshwater parameter η_2, since for certain values multiple steady states exist. To find the regime of η_2 for which these multiple equilibria exist, we consider the steady equations by setting the time derivatives of equations 2.2 to zero. Solving for T and S as a function of the parameters

η_1, η_2 and η_3 then gives

$$T = \frac{\eta_1}{1 + |\Psi|},$$
$$S = \frac{\eta_2}{\eta_3 + |\Psi|}.$$

We can now solve these equations for different values of η_1 and η_2 and draw a regime diagram. The regime diagram shows us which solutions exist for certain parameter values, it is shown in figure 2.2.

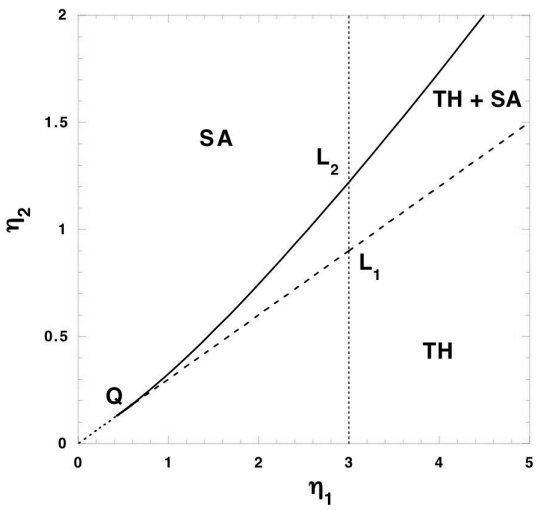

Figure 2.2: Regime diagram where the boundaries of the different solutions of the Stommel two-box model are plotted in the parameter space of η_1 and η_2. The dashed line at $\eta_1 = 3.0$ can be used for comparison with figure 2.3. Figure from Dijkstra (2005).

In figure 2.2, two curves L_1 and L_2 have been indicated. To the right of the curve L_1 there is a unique TH solution, with polar sinking and positive Ψ. To the left of curve L_2 there is a unique SA solution, with equatorial sinking and negative Ψ. In the area bounded by the curves L_1 and L_2 however, multiple steady solutions exist and both the TH and the SA solution occur.

To investigate the stability of the steady solution $\bar{T}$ and $\bar{S}$, we add perturbations $\tilde{T}$ and $\tilde{S}$, such that $T = \bar{T} + \tilde{T}$ and $S = \bar{S} + \tilde{S}$. If we substitute these expressions for T and S into the evolution equations 2.2, we get an eigenvalue problem that admits solutions of the form

$$\tilde{T} = \hat{T}e^{\sigma t},$$
$$\tilde{S} = \hat{S}e^{\sigma t}.$$

Here $\hat{T}$ and $\hat{S}$ are eigenvectors of the temperature and salinity respectively and $\sigma = \sigma_r + i\sigma_i$ is the eigenvalue and complex growth factor. The real part σ_r determines the damping ($\sigma_r < 0$) or growth ($\sigma_r > 0$) of the perturbations. So by considering the value of σ_r, we can conclude if a steady solution is stable or unstable.

Figure 2.3 shows the bifurcation diagram of the two-box model, in which the steady flow $\bar{\Psi}$ is plotted against the freshwater parameter η_2. This illustrates the occurrence of multiple steady states as we saw in the regime diagram in figure 2.2 in a different way. In the bifurcation diagram, the value of $\eta_1 = 3.0$ and is fixed. This is shown by the dotted line in figure 2.2. We again see the points L_1 and L_2 in figure 2.3. The signs of the real eigenvalues of the temperature and salinity are shown along the branches.

For values of η_2 up to point L_2 a stable TH solution exists. Similarly, for values of η_2 beyond L_1 there is a stable SA solution. In these cases, both of the eigenvalues are negative and hence perturbations are damped. In between the points L_1 and L_2 however, one of the eigenvalues is positive and the solution becomes unstable. We also see that multiple steady states exist for values of η_2 between about 0.8 and 1.2, here the stable TH and SA states overlap.

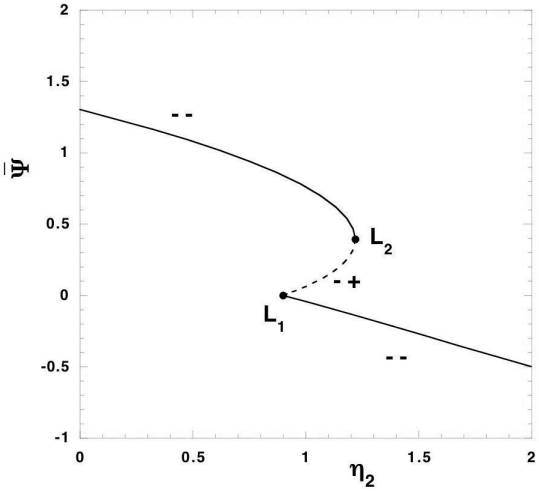

Figure 2.3: Bifurcation diagram of the Stommel two-box model. The steady flow $\bar{\Psi}$ is plotted for a varying parameter η_2. The parameter values $\eta_1 = 3.0$ and $\eta_3 = 0.3$ are fixed. The $\pm$ signs along the branches indicate the sign of the real eigenvalue σ_r. The drawn curves indicate stable steady solutions, dashed curves unstable steady solutions. The points L_1 and L_2 indicate the transitions from a stable to an unstable solution and are the same as those shown in figure 2.2. Figure from Dijkstra (2005).

2.1.2 Stommel three-box model

We can extend the Stommel two-box model by including a third polar box, as done by Thual and McWilliams (1992). The boxes are again connected at the surface and the bottom of each box. The three-box model is sketched in figure 2.4.

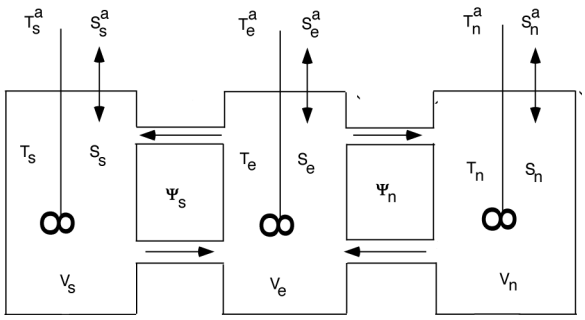

Figure 2.4: Sketch of the Stommel three-box model. An equatorial, a southern and a northern polar box contain well mixed water and are connected at the surface and at the bottom of each box. As in the Stommel two-box model the circulation is set up by density gradients. Figure from Dijkstra (2005).

The southern polar box is denoted by the subscript s and the northern polar box by n. The dimensional evolution equations are an extension of the equations 2.1 and are given by

$$V_s \frac{dT_{s*}}{dt_*} = C_s^T (T_s^a - T_{s*}) + |\Psi_{s*}|(T_{e*} - T_{s*}), \tag{2.6a}$$

$$V_e \frac{dT_{e*}}{dt_*} = C_e^T (T_e^a - T_{e*}) + |\Psi_{s*}|(T_{s*} - T_{e*}) + |\Psi_{n*}|(T_{n*} - T_{e*}), \tag{2.6b}$$

$$V_n \frac{dT_{n*}}{dt_*} = C_n^T (T_n^a - T_{n*}) + |\Psi_{n*}|(T_{e*} - T_{n*}), \tag{2.6c}$$

$$V_s \frac{dS_{s*}}{dt_*} = C_s^S (S_s^a - S_{s*}) + |\Psi_{s*}|(S_{e*} - S_{s*}), \tag{2.6d}$$

$$V_e \frac{dS_{e*}}{dt_*} = C_e^S (S_e^a - S_{e*}) + |\Psi_{s*}|(S_{s*} - S_{e*}) + |\Psi_{n*}|(S_{n*} - S_{e*}), \tag{2.6e}$$

$$V_n \frac{dS_{n*}}{dt_*} = C_n^S (S_n^a - S_{n*}) + |\Psi_{n*}|(S_{e*} - S_{n*}), \tag{2.6f}$$

with the flow rates

$$\Psi_{s*} = \lambda(\alpha_T(T_{e*} - T_{s*}) - \alpha_S(S_{e*} - S_{s*})),$$
$$\Psi_{n*} = \lambda(\alpha_T(T_{e*} - T_{n*}) - \alpha_S(S_{e*} - S_{n*})).$$

As was the case for the two-box model, the sign of each flow rate is positive when the surface flow is directed from equator to pole. For simplicity, we again assume that $\frac{C_s^T}{V_s} = \frac{C_e^T}{V_e} = \frac{C_n^T}{V_n} \equiv R_T$ and $\frac{C_s^S}{V_s} = \frac{C_e^S}{V_e} = \frac{C_n^S}{V_n} \equiv R_S$. We introduce the new variables $\Theta_{s*} = T_{e*} - T_{s*}$, $\Theta_{n*} = T_{e*} - T_{n*}$, $\Sigma_{s*} = S_{e*} - S_{s*}$ and $\Sigma_{n*} = S_{e*} - S_{n*}$. We can then find the dimensionless equations by scaling Θ_*, Σ_* and time with $\frac{V_s R_T}{2\lambda\alpha_T}$, $\frac{2V_s R_T}{2\lambda\alpha_S}$ and R_T^{-1}, respectively. For $V_s = V_n = \frac{V_e}{2}$ we then get

$$\frac{d\Theta_s}{dt} = \alpha_s - \Theta_s(1 + \frac{3}{4}|\Psi_s|) - \frac{1}{4}|\Psi_n|\Theta_n, \tag{2.8a}$$
$$\frac{d\Theta_n}{dt} = \alpha_n - \Theta_n(1 + \frac{3}{4}|\Psi_n|) - \frac{1}{4}|\Psi_s|\Theta_s, \tag{2.8b}$$
$$\frac{d\Sigma_s}{dt} = \beta_s - \Sigma_s(\eta_3 + \frac{3}{4}|\Psi_s|) - \frac{1}{4}|\Psi_n|\Sigma_n, \tag{2.8c}$$
$$\frac{d\Sigma_n}{dt} = \beta_n - \Sigma_n(\eta_3 + \frac{3}{4}|\Psi_n|) - \frac{1}{4}|\Psi_s|\Sigma_s. \tag{2.8d}$$

Here $\Psi_s = \Theta_s - \Sigma_s$ and $\Psi_n = \Theta_n - \Sigma_n$. The parameter $\eta_3 = \frac{R_S}{R_T}$ as before, α_n and α_s are thermal parameters and β_s and β_n are saline parameters given by

$$\alpha_s = \frac{2\lambda\alpha_T}{V_s R_T}(T_e^a - T_s^a),$$
$$\alpha_n = \frac{2\lambda\alpha_T}{V_s R_T}(T_e^a - T_n^a),$$

$$\beta_s = \frac{R_S}{R_T}\frac{2\lambda\alpha_S}{V_s R_T}(S_e^a - S_s^a),$$
$$\beta_n = \frac{R_S}{R_T}\frac{2\lambda\alpha_S}{V_s R_T}(S_e^a - S_n^a).$$

If $\alpha_s = \alpha_n$ and $\beta_s = \beta_n$, then the forcing is symmetric with respect to the equator. In this case, the north and south are indistinguishable in the model. To show the structure and stability of the steady solutions, we again plot a bifurcation diagram in figure 2.5.

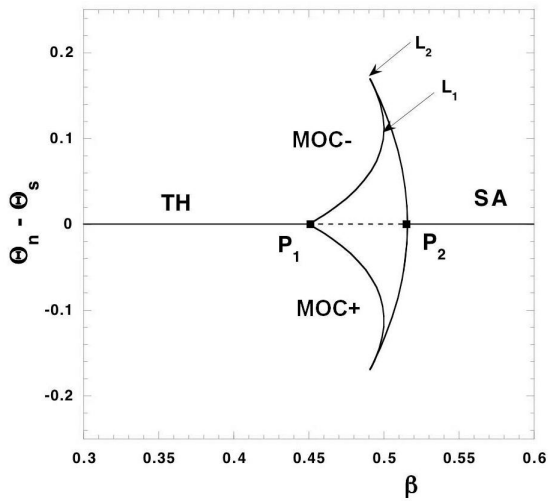

Figure 2.5: Bifurcation diagram of the Stommel three-box model with symmetric forcing $\alpha_s = \alpha_n = \alpha = 1.5$, $\beta_s = \beta_n = \beta$ and $\eta_3 = 0.3$. The parameter β is used as a control parameter and $\Theta_n - \Theta_s$ is plotted along the vertical axis. The quantity $\Theta_n - \Theta_s$ is zero when the solutions are symmetric with respect to the equator. Again, the drawn curve indicates stable steady solutions, the dashed curve unstable steady solutions. The points P_1 and P_2 indicate the transition points between stable and unstable solutions and the points L_1 and L_2 are also shown. Next to the branches, the solutions TH, SA, NPP and SPP which are illustrated in figure 2.6 are indicated. Figure from Dijkstra (2005).

The bifurcation diagram has been plotted with a fixed value for $\alpha_s = \alpha_n = 1.5$ and by using $\beta_s = \beta_n = \beta$ as a control parameter. The difference $\Theta_n - \Theta_s$ is plotted against β and was chosen because it is zero for equatorially symmetric solutions. For small β we see that there is only one symmetric solution, which is the TH solution. At the point P_1 the TH solution becomes unstable and two equatorially asymmetric solutions appear. In case of these asymmetric solutions, there is no longer any down- or upwelling at the equator, only at the poles. We call the solution with downwelling in the north, so positive Ψ_n, the MOC+ solution and with downwelling in the south, so negative Ψ_n, the MOC- solution. For values of β beyond point P_2 the stable symmetric SA solution exists. The four possible solutions are illustrated in figure 2.6.

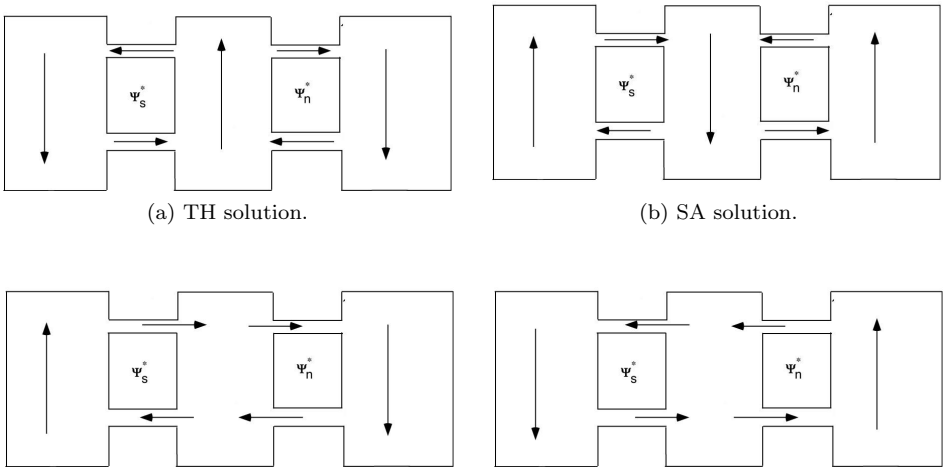

(a) TH solution. (b) SA solution.

(c) MOC+ solution. (d) MOC- solution.

Figure 2.6: Sketch of the four possible solutions of the Stommel three-box model. Figure from Dijkstra (2005).

When $\alpha_n \neq \alpha_s$ or $\beta_n \neq \beta_s$ the equatorial symmetry of the system is no longer present. We consider the asymmetrical case with a larger freshwater flux in the northern hemisphere, so $\alpha_n = \alpha_s = \alpha$ and $\beta_n = \beta_s(1+\epsilon)$. In this case, the density is decreased in the north and for a flow driven purely by the freshwater flux, there is a preference for southern sinking. When the asymmetry in the system is large enough, we see that the points P_1 and P_2 in the bifurcation diagram in figure 2.5 disappear. Instead, what remains is a transition from the MOC+ solution to the MOC- solution via the tipping points L_1 and L_2 when the freshwater flux increases. A sketch of this bifurcation diagram is shown in figure 2.7. We will consider this bifurcation diagram in more detail in chapter 5.

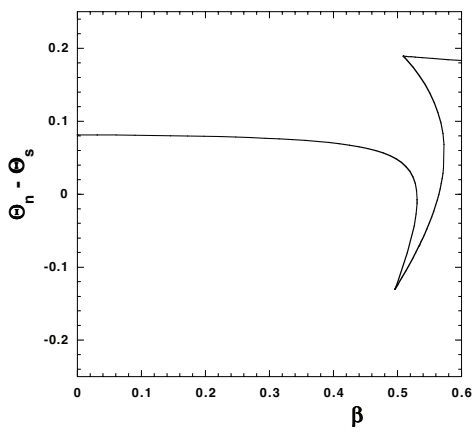

Figure 2.7: Sketch of the bifurcation diagram of the Stommel three-box model with asymmetric forcing $\beta_n = \beta_s(1+\epsilon)$ for $\epsilon > 0$. The stability of the states is not shown. Figure from Dijkstra (2005).

2.1.3 Physical mechanisms

In both the Stommel two- and three-box models we saw that multiple equilibria of the Meridional Overturning Circulation exist. An important physical mechanism that can cause the overlap of steady states is the salt-advection feedback. To illustrate the effect of this feedback, we consider the TH solution in the northern hemisphere. In this case, there is sinking at the pole and the surface flow is directed from the equator to the north. The waters at low latitudes are warmer and more saline than at high latitudes. Because of this, there is northward heat and salt transport. The enhanced salt transport increases the density of the polar waters, which strengthens the circulation. On the other hand, the transport of heat lowers the density of the polar waters and therefore provides a negative feedback on the circulation.

In addition to the advection feedback, the different damping times of salinity and temperature anomalies are central to the existence of multiple steady states. As we saw in the two- and three-box models, the relaxation coefficients of temperature R_T and salinity R_S are not equal to each other. If we define the response time scales of temperature and salinity as $\tau_T = \frac{1}{R_T}$ and $\tau_S = \frac{1}{R_S}$ respectively, then the parameter $\eta_3 = \frac{R_S}{R_T} = \frac{\tau_T}{\tau_S}$ and $\eta_3 < 1$. This indicates that the damping time of temperature anomalies is fast; the atmosphere exerts a strong control on the sea surface temperature anomalies. On the other hand, the response time τ_S is slow, salinity anomalies in the ocean do not affect the freshwater flux.

These different response times combined with the advection feedback provide a transition mechanism of the Meridional Overturning Circulation. For example, imagine that a surface freshwater anomaly is present in the northern part of the TH solution. Because the density of the water decreases in the north, the strength of the circulation also decreases. This means that the northward transport of heat and salt also diminishes. The negative temperature anomaly is rapidly damped at the sea surface, but the freshwater perturbation is not damped. Therefore, the circulation continues to decrease and this positive feedback results in a rapid decline in strength of the MOC and possibly a transition to a different solution.

2.2 Bifurcations

The equations 2.2 and 2.8 that govern the evolution of temperature and salinity in the Stommel two- and three-box models both form a set of ordinary differential equations

$$\frac{d\mathbf{x}}{dt} = f(\mathbf{x}),$$

where $\mathbf{x}$ represents a parameter, in our case temperature T or salinity S, and f is a function that does not depend explicitly on time. A solution $\bar{\mathbf{x}}$ of this system is a fixed point if

$$f(\bar{\mathbf{x}}) = 0. \tag{2.11}$$

Therefore, a fixed point represents an equilibrium solution of the system, since equation 2.11 implies that $\frac{d\bar{\mathbf{x}}}{dt} = 0$. As we saw earlier, stable and unstable steady states, and so fixed points, exist. We can investigate the stability of the fixed points by adding a perturbation $\tilde{\mathbf{x}}$ such that $\mathbf{x} = \bar{\mathbf{x}} + \tilde{\mathbf{x}}$. Solving this system again gives an eigenvalue problem with solutions of the form $\tilde{\mathbf{x}} = \hat{\mathbf{x}}e^{\sigma t}$. As before, $\hat{\mathbf{x}}$ is the eigenvector, $\sigma = \sigma_r + i\sigma_i$ is the complex growth factor and the sign of σ_r determines the damping or growth of a perturbation. Stable fixed points act as attractors, the solution is attracted towards them. On the other hand, unstable fixed points act as repellers, the solution diverges away from these points.

Fixed points can be created or destroyed, or their stability can change. Such a qualitative change is called a bifurcation and the parameter values at which they occur are bifurcation points. Bifurcations are important because they provide modes of transition as a control parameter is varied. A bifurcation that needs at least m parameters to occur is called a codimension-m bifurcation. In case of the Stommel two- and three-box models only one parameter, η_2 and β respectively, was required for bifurcations to occur. So the bifurcations in the box models are of codimension-1.

Transition behaviour can occur in several different ways, depending on how the eigenvalues σ cross the imaginary axis. In case of a codimension-1 bifurcation, a single real eigenvalue σ_r or a complex conjugate pair of eigenvalues can cross the axis. Here, we will only focus on the bifurcations that occur in the Stommel two- and three-box models, which take place due to the crossing of a real eigenvalue. The two bifurcations that we saw in the box models are the saddle-node bifurcation and the pitchfork bifurcation.

2.2.1 Saddle-node bifurcation

In a saddle-node bifurcation, fixed points are created and destroyed. As the control parameter is varied, a stable and an unstable fixed point move towards each other, collide and mutually annihilate.

To describe a bifurcation mathematically, normal forms are used. In general, a normal form is a simplified form of a mathematical object. In this case, the idea is that close to a bifurcation point, the dynamics look like the normal form of the specific bifurcation. The normal form of a saddle-node bifurcation is given by

$$\dot{x} = r + \delta x, \tag{2.12}$$

where $\dot{x}$ indicates the time-derivative of x, $\delta \in \{-1, 1\}$ and the parameter r can be both positive or negative. When $\delta = +1$, steady solutions $\bar{x} = \pm\sqrt{-r}$ only exist for $r < 0$, as is shown in figure 2.8a. In this case, there are two fixed points, one stable and one unstable. As r approaches zero, the two fixed points move towards each other. When $r = 0$, the stable and unstable fixed points merge into a half-stable point in figure 2.8b. As soon as $r > 0$ the fixed point vanishes entirely, shown in figure 2.8c. In this example, a bifurcation occurred at $r = 0$.

So, for $\delta = +1$, fixed points only exist when $r < 0$. The steady solution is stable when $\bar{x} = -\sqrt{r}$ and unstable when $\bar{x} = \sqrt{r}$. For $\delta = -1$ a similar situation arises. Steady solutions $\bar{x} = \pm\sqrt{r}$ only exist for $r > 0$. In this case, the solution $\bar{x} = \sqrt{r}$ is stable and $\bar{x} = -\sqrt{r}$ is unstable. The bifurcation diagrams of the saddle-node bifurcation for both $\delta = +1$ and $\delta = -1$ are shown in figure 2.9.

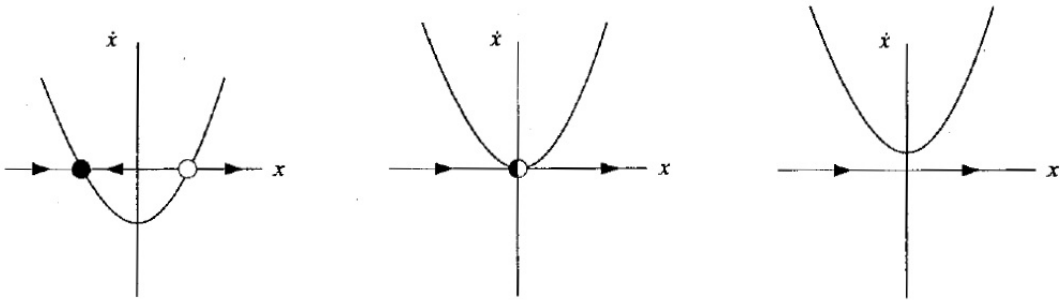

(a) $r < 0$ (b) $r = 0$ (c) $r > 0$

Figure 2.8: Illustration of a saddle-node bifurcation. Solutions of equation 2.12 for $\delta = +1$ and different values of r are shown. Fixed points are indicated by filled circles (stable) and open circles (unstable). Figure from Strogatz (1994).

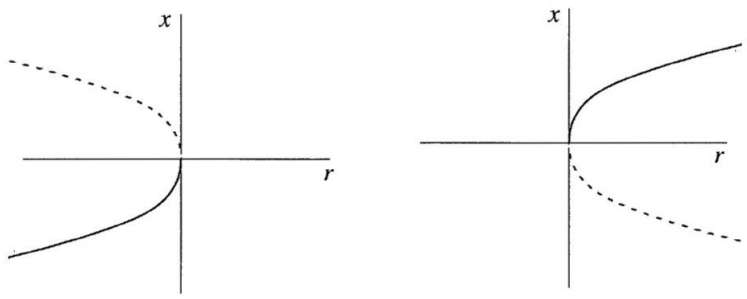

(a) (b)

Figure 2.9: Bifurcation diagram of the saddle-node bifurcation for (a) $\delta = +1$ and (b) $\delta = -1$. The drawn curve indicates stable steady solutions, the dashed curve unstable steady solutions. Figure from Strogatz (1994).

A saddle-node bifurcation occurred in both the Stommel two- and three-box model. The points L_1 and L_2 in figures 2.3 and 2.5 are examples of a saddle-node bifurcation.

2.2.2 Pitchfork bifurcation

The pitchfork bifurcation is common in physical problems that contain symmetry. The Stommel three-box model with symmetrical forcing is such a problem. In this case, fixed points tend to appear and disappear in symmetrical pairs. The normal form is given by

$$\dot{x} = rx - \delta x^3. \tag{2.13}$$

Two different types of pitchfork bifurcations exist, when $\delta = +1$ the bifurcation is a supercritical pitchfork. If we again consider the fixed points for different values of r, we see that for $r < 0$ there is one stable steady state $\bar{x} = 0$, shown in figure 2.10a. When $r = 0$, shown in figure 2.10b, the origin is still a stable point, but more weakly. For $r > 0$ the origin becomes unstable and two new stable fixed points appear, see figure 2.10c. These stable solutions are $\bar{x} = \pm\sqrt{r}$.

The bifurcation diagram of the supercritical pitchfork is shown in figure 2.11a. From this figure, the name pitchfork immediately becomes clear.

For $\delta = -1$ we have a subcritical pitchfork bifurcation. This bifurcation diagram is shown in figure 2.11b. Since this type of bifurcation does not occur in either of our box models, we do not consider it any further here.

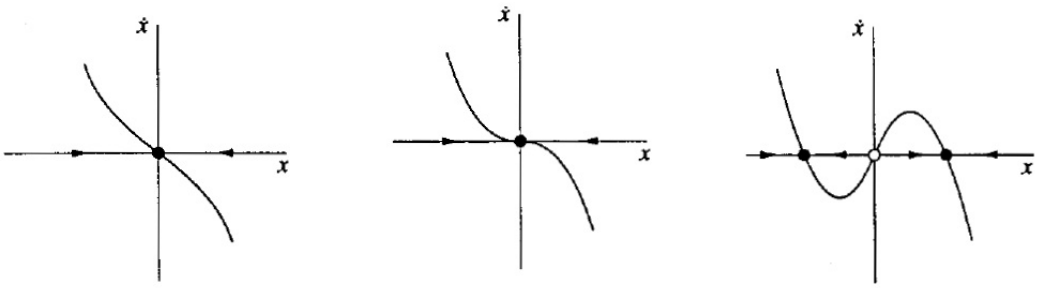

(a) $r < 0$ (b) $r = 0$ (c) $r > 0$

Figure 2.10: Illustration of a supercritical pitchfork bifurcation. Solutions of equation 2.13 for $\delta = +1$ and different values of r are shown. Fixed points are indicated by filled circles (stable) and open circles (unstable). Figure from Strogatz (1994).

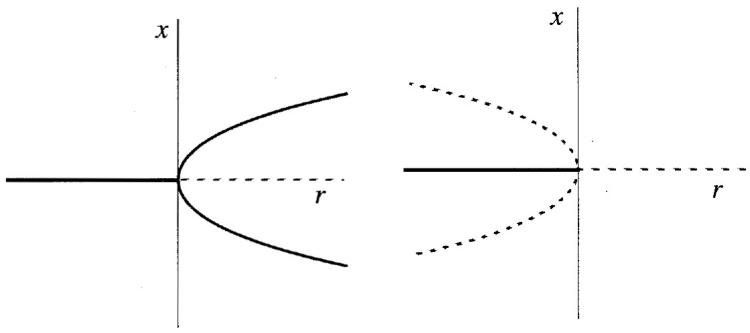

(a) (b)

Figure 2.11: Bifurcation diagram of (a) the supercritical pitchfork bifurcation with $\delta = +1$ and (b) the subcritical pitchfork bifurcation with $\delta = -1$. The drawn curve indicates stable steady solutions, the dashed curve unstable steady solutions. Figure from Strogatz (1994).

The supercritical pitchfork bifurcation occurs in the Stommel three-box model. The points P_1 and P_2 in figure 2.5 are both bifurcations of this type.

In summary, we have seen that multiple steady states exist in both the Stommel two- and three-box models. In case of the three-box model two equatorially symmetric and two asymmetric solutions exist under symmetric forcing conditions. The steady solutions can be either stable or unstable. Transition between different states occurs at pitchfork and saddle-node bifurcation points when the freshwater flux is varied. Under asymmetric forcing conditions (increased freshwater input in the north) the pitchfork bifurcations disappear and transitions between the MOC+ and MOC- solutions occur at saddle-node bifurcation points.

Chapter 3

Model and Method

In this chapter we describe THCM, which we use to model the Meridional Overturning Circulation, as well as the software used to construct networks. The method for network construction is also explained.

3.1 THCM

As we saw in the previous chapter, multiple steady states of the MOC exist under certain conditions. In model simulations, these multiple equilibria can be found by slowly varying the freshwater flux. The corresponding bifurcation diagram then shows transitions from one stable state to another. In the transient behaviour of the flow, unstable steady states are important. Therefore, we want to use a model that can determine and follow these unstable states in parameter space. This can be done with the ThermoHaline Circulation Model (THCM, den Toom et al. (2011)), which is a fully implicit ocean model.

In this study, we consider the meridional-depth plane and therefore use a two-dimensional adaptation of THCM with no wind-stress forcing and zero rotation. The governing model equations are the hydrostatic primitive equations, given by

$$
\begin{aligned}
0 &= -\frac{1}{\rho_0 r_0}\frac{\partial p_*}{\partial \theta_*} + A_V \frac{\partial^2 v_*}{\partial z_*^2} + \frac{A_H}{r_0^2}\left(\frac{1}{\cos\theta_*}\frac{\partial}{\partial\theta_*}\left(\cos\theta_*\frac{\partial v_*}{\partial\theta_*}\right) + (1-\tan^2\theta_*)v_*\right),\\
\frac{\partial p_*}{\partial z_*} &= -\rho_* g,\\
0 &= \frac{\partial w_*}{\partial z_*} + \frac{1}{r_0}\frac{\partial v_*}{\partial\theta_*} - \frac{v_*\tan\theta_*}{r_0},\\
\frac{dT_*}{dt_*} &= \frac{K_H}{r_0^2\cos\theta_*}\frac{\partial}{\partial\theta_*}\left(\frac{\partial T_*}{\partial\theta_*}\cos\theta_*\right) + K_V\frac{\partial^2 T_*}{\partial z_*^2},\\
\frac{dS_*}{dt_*} &= \frac{K_H}{r_0^2\cos\theta_*}\frac{\partial}{\partial\theta_*}\left(\frac{\partial S_*}{\partial\theta_*}\cos\theta_*\right) + K_V\frac{\partial^2 S_*}{\partial z_*^2}.
\end{aligned}
$$

Here, $\frac{d}{dt_*} = \frac{\partial}{\partial t_*} + \frac{v_*}{r_0}\frac{\partial}{\partial\theta_*} + w_*\frac{\partial}{\partial z_*}$ is the material derivative, θ_* the latitude and z_* depth. The radius of the Earth is represented by r_0, v_* and w_* are the meridional and vertical velocity components respectively, pressure is represented by p_*, temperature by T_* and salinity by S_*. The density ρ_* is related to the temperature and salinity by the linear equation of state

$$\rho_* = \rho_0(1 - \alpha_T(T_* - T_0) + \alpha_S(S_* - S_0)),$$

with expansion coefficients α_T and α_S and reference temperature T_0, salinity S_0 and density ρ_0.

Furthermore, mixing is represented by eddy diffusivities, with horizontal and vertical diffusivities K_H and K_V for both heat and salt and friction coefficients A_H and A_V for momentum. At the lateral and bottom boundaries, no-slip and no-flux conditions are imposed. Standard values for the parameters in these equations are shown in table 3.1.

$r_0 = 6.37 \times 10^6$ m	$\rho_0 = 1.0 \times 10^3$ kg m^{-3}
$g = 9.8$ ms^{-2}	$\alpha_T = 1.0 \times 10^{-4}$ K^{-1}
$A_H = 2.2 \times 10^{12}$ m^{2}s^{-1}	$\alpha_S = 7.6 \times 10^{-4}$ psu^{-1}
$A_V = 1.0 \times 10^{-3}$ m^{2}s^{-1}	$T_0 = 15.0$°C
$K_H = 1.0 \times 10^3$ m^{2}s^{-1}	$S_0 = 35.0$ psu
$K_V = 1.0 \times 10^{-4} K^{-1}$	$H = 4000$ m
$\theta_N = 60°$	

Table 3.1: Parameter values of the two-dimensional model.

At the ocean-atmosphere interface mixed boundary conditions are imposed. The surface temperature is restored to a temperature profile T_S,

$$T_S = T_0 + \frac{\Delta T}{2} \cos\left(\frac{\pi\theta}{\theta_N}\right),$$

where $\Delta T = 20$°C and the basin is bounded meridionally by $[-\theta_N, \theta_N]$ and vertically by $[-H, 0]$.

We consider two different cases of freshwater forcing F_S, a symmetrical and an asymmetrical forcing with a larger freshwater flux in the northern hemisphere. In the symmetrical case, the freshwater forcing is prescribed as a virtual salinity flux by

$$F_S = \beta \frac{\cos\left(\frac{\pi\theta}{\theta_N}\right)}{\cos(\theta)}. \tag{3.2}$$

In this case, the amplitude of the freshwater forcing β is the control parameter. The asymmetrical freshwater forcing is also prescribed as a virtual salinity flux by

$$F_S = \beta \frac{\cos\left(\frac{\pi\theta}{\theta_N}\right)}{\cos(\theta)} + \beta_n F_p(\theta). \tag{3.3}$$

Here, β is the amplitude of the background freshwater forcing and β_n is the strength of the anomalous freshwater flux which is only added over the area $[40°\text{N}, 60°\text{N}]$ (where $F_p = 1$ and it is zero elsewhere). In the asymmetrical case, β_n is our control parameter.

The equations are discretised in space using an Arakawa B-grid that places the p, T and S points in the center of a grid cell and the v and w points on its boundaries, as is described by den Toom et al. (2011). To calculate branches of steady states directly as a function of the control parameter, pseudo-arclength continuation is used. With this technique, unstable solutions can also be determined, so that a full bifurcation diagram can be computed. To converge to individual solutions, the Newton-Raphson method is employed. The model also implements the Jacobi-Davidson QZ method to solve linear stability problems.

The model domain is a meridional-depth plane that is bounded by the latitudes 60°S and 60°N, so $\theta_N = 60°$, and has a constant depth of $H = 4000$ m. This cross-section is located in the Atlantic Ocean and has a width of 64°, which is relevant for the value of the strength of the MOC. Our grid contains 32 points in the meridional direction and 16 points in the vertical direction. That gives us a meridional resolution of 3.75° and 16 vertical layers with a thickness of 250 m.

3.2 Network construction

Using the software "pynetwork" created by Donges et al. (2012), we construct networks from the data obtained from THCM.

Suppose that our data is contained in a matrix F, ordered in such a way that each column p_i at a grid point contains a time series of length n (for example of the temperature or salinity). The data in F has been detrended and the mean of each time series removed. Following several climate studies (for example Donges et al. (2009)), the linear Pearson correlation coefficient with zero lag can be used to determine the correlation between two grid points. The correlation matrix r is then given by

$$r_{ij} = \frac{\sum_{t=1}^{n} p_i(t)p_j(t)}{\sum_{t=1}^{n} p_i^2(t) \sum_{t=1}^{n} p_j^2(t)}, \tag{3.4}$$

where the subscript ij indicates the element of the matrix on the ith column and the jth row.

Each grid point can be seen as a node in the network. From the correlation coefficient r_{ij} we can set up links between each pair of nodes. We consider points that are sufficiently correlated or anti-correlated as linked. To determine when two nodes are connected, we set a threshold value τ. If the absolute value of the correlation coefficient between two points is above the threshold, then these points are linked. All links are contained in the adjacency matrix A, which can be determined from the correlation matrix r as

$$A_{ij} = H(|r_{ij}| - \tau),$$

where H is the Heaviside function.

3.2.1 Network properties

We have now constructed a network from our data matrix F. The network topology can be investigated with the help of several useful properties.

Distance and closeness

In a network, the 'distance' between two nodes is measured by the number of links that have to be 'crossed' to get from one node to the other. The link distance is then given by the shortest path between two nodes. The farness of a node can be found by computing the sum of its link distances to all other nodes. The closeness is then defined as the inverse of the farness. So, a node with a low closeness has a low total distance to all other nodes. Therefore, the closeness measures how central a node is in the network.

Degree

A measure for the total connectedness of a node is given by the degree d. This can be calculated from

$$d_i = \sum_{j=1}^{N} A_{ij}, \tag{3.5}$$

where N is the total number of nodes. The degree shows the total number of links that a node possesses. Therefore, a high degree means that a certain node is connected to a large amount of other nodes in the network, whereas a low degree indicates that a node is more 'isolated' from the rest of the network. In this thesis, we will focus on the degree d.

Clustering

The extent to which nodes cluster together in a network is measured by the clustering coefficient c. The computation of the clustering coefficient is illustrated with an example in figure 3.1. Figure 3.1a shows the links of a node i, in this case i is connected to eight other nodes. These eight nodes define the closest neighbourhood of i (where node i itself is not part of the neighbourhood).
We then consider the links between these neighbours Δ_i, illustrated in figure 3.1b. In this example $\Delta_i = 5$. For a number of k_i neighbours the total possible connections between them is $\frac{k_i(k_i-1)}{2}$. The clustering coefficient of node i is then defined as

$$c_i = \frac{2\Delta_i}{k_i(k_i - 1)}.$$

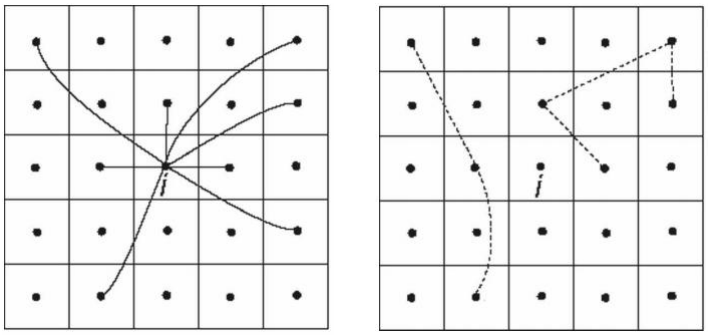

(a) (b)

Figure 3.1: Illustration of the method used to find the clustering coefficient of a node i. (a) Links of node i. (b) Links within the neighbourhood of i. Figure from Tsonis et al. (2008).

It follows that a high clustering coefficient indicates that a lot of nodes in the neighbourhood are connected to each other; there is high clustering. Some modifications on the exact definition of the clustering coefficient also exist, see for example Tsonis et al. (2008).

Betweenness

The degree and closeness give us a general idea of how well connected a node is. The importance of a specific node for the connectedness of the entire network is quantified by the betweenness b, which is defined as

$$b_p = \sum_{i,j \neq p}^{N} \frac{\sigma_{ij}(p)}{\sigma_{ij}}.$$

Here, σ_{ij} is the total number of shortest paths from node i to j and $\sigma_{ij}(p)$ is the number of those paths that pass through the node p. So, the betweenness of a specific node p is given by the fraction of shortest paths that go through the node. Therefore, a high betweenness indicates that a node is important for all connections in the network. For example, in a highly clustered network, nodes that provide connections between different clusters will have a high betweenness.

Chapter 4

Results: Symmetrical forcing

In this chapter, we consider the symmetrically forced MOC. We construct the bifurcation diagram of the MOC and create temperature and salinity data at different points along the diagram. From these data we construct networks and consider the evolution of the network topology when approaching the tipping point. To provide an explanation for the change in the network topology, we investigate the eigenvectors and empirical orthogonal functions (EOFs) of the system. We then consider networks constructed from grids with a limited amount of nodes and define an indicator for an early warning signal.

4.1 Bifurcation diagram

We saw in section 2 that the Meridional Overturning Circulation behaves in a similar fashion as the Stommel three-box model. As in the box model, multiple steady states of the MOC exist. Here we consider symmetrical forcing with a freshwater flux as described in equation 3.2. We can then find the multiple states of the system with THCM by varying the freshwater parameter β. The dynamical behaviour of the system is shown in the bifurcation diagram in figure 4.1. In this figure, the maximum of the meridional overturning streamfunction Ψ_M is plotted against the freshwater parameter β. Notice that this diagram is qualitatively similar to the bifurcation diagram of the Stommel three-box model in figure 2.5.
For each value of β there is an equatorially symmetric solution, which is stable except between the two pitchfork bifurcations, indicated by points P in figure 4.1. For $\beta \leq 0.175$ m yr^{-1} the symmetric state is the TH solution, with sinking at the poles, for $\beta \geq 0.175$ m yr^{-1} it is the SA solution, with sinking at the equator. The two equatorially asymmetric solutions are connected by the pitchfork bifurcations. They are stable between the first pitchfork and the saddle-node bifurcations, indicated by an S in figure 4.1.

On the right of figure 4.1 a plot of the steady state MOC is shown for all three branches of the bifurcation diagram. With the symmetric branch containing the TH- and SA solution and two asymmetric branches with the MOC+ solution (upper branch, positive Ψ, sinking in the north) and the MOC- solution (lower branch, negative Ψ, sinking in the south).

Four points have been indicated with stars along the positive asymmetrical branch of the bifurcation diagram in figure 4.1. Point 1 is the farthest away from the saddle-node bifurcation, with each of the successive points approaching it more closely. The coordinates of these points are given in table 4.1. The saddle-node is the transition point between a stable steady solution and an unstable solution. If the freshwater parameter β is increased to a value beyond the saddle-node bifurcation, the system will rapidly diverge away from the positive asymmetric solution towards the symmetric SA solution. Such an abrupt change is known as a tipping point. From now on, we will refer to the saddle-node bifurcation on the positive asymmetrical branch of the bifurcation diagram as the tipping point S of the MOC.
At each of these four points we want to create a time series of temperature and salinity. Since the system is in a stable steady state, we add a reproducible random white noise perturbation to the forcing in order to get a useful time series. The freshwater forcing F_S from equation 3.2 then becomes

$$F_S = \beta \frac{\cos\left(\frac{\pi\theta}{\theta_N}\right)}{\cos(\theta)} + \Delta w_r(\theta, t),$$

where w_r is the white noise perturbation that depends on latitude θ and time t and $Delta = 0.1$ is the amplitude of the perturbation w_r.

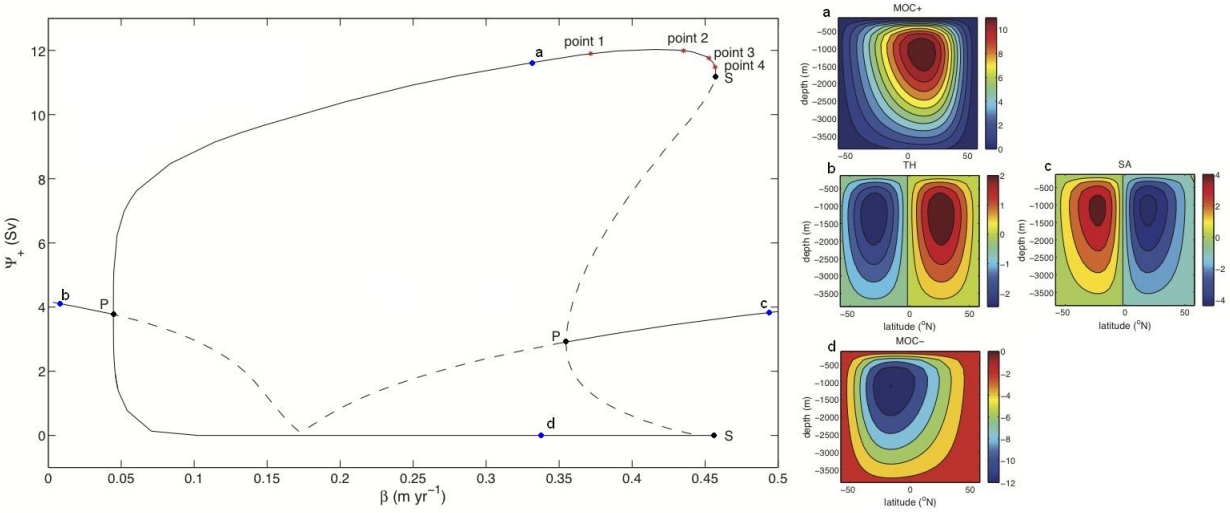

Figure 4.1: Left: Bifurcation diagram of the symmetrically forced MOC. The maximum of the meridional overturning streamfunction is shown against the freshwater flux parameter β. The symmetrical branch and two asymmetrical branches are shown. Stable steady solutions are indicated by drawn curves, unstable steady solutions by dashed curves. Points P indicate pitchfork bifurcations, points S saddle-node bifurcations. Points 1 to 4 are indicated for future reference. Right: Examples of the steady state MOC in the latitude-depth plane are shown for each of the three branches of the bifurcation diagram. Locations where the examples were taken are indicated by blue points labeled with a, b, c and d in the bifurcation diagram.

	β m yr^{-1}	Ψ_M(Sv)
point 1	0.371	11.9
point 2	0.435	12.0
point 3	0.453	11.8
point 4	0.456	11.5

Table 4.1: Coordinates of the four points approaching the tipping point S indicated on the bifurcation diagram.

We create datasets that cover periods of 500 years, with a resolution of 1 year. An example of the time series created in this way is shown in figure 4.2. Typical steady state temperature and salinity profiles at each of the four points are also shown in this figure. From these time series, networks can be constructed and their properties when approaching the tipping point analysed.

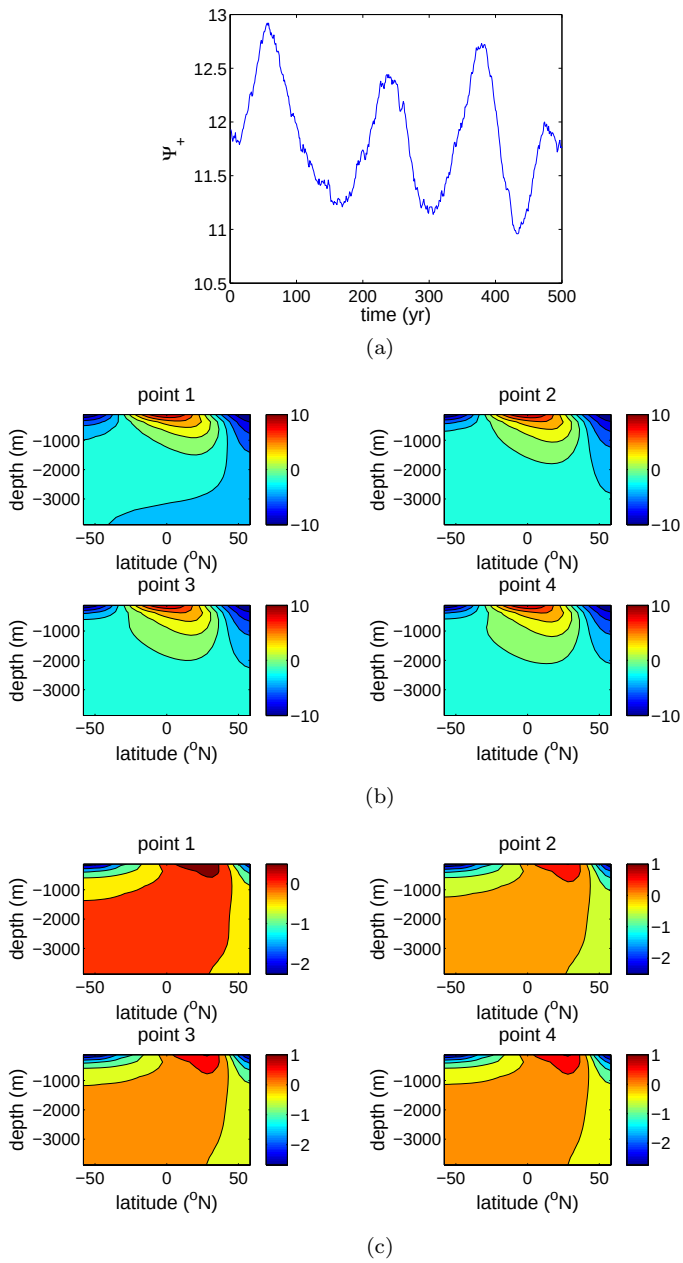

Figure 4.2: (a) Example time series (constructed in point 1 on the bifurcation diagram) of the maximum of the streamfunction created by adding white noise to the forcing. Steady state temperature (b) and salinity (c) profiles at each of the four points approaching the tipping point.

4.2 Networks

At each of the four points indicated in figure 4.1 we construct networks from both the temperature and the salinity data, using a threshold value of $\tau = 0.7$. The evolution of the topology can be investigated by considering several network properties. Here, we have chosen to look at the degree, since this shows the most obvious evolution when approaching the tipping point and because the degree is relatively simple to understand intuitively. Figures 4.3 and 4.4 show the degree of the temperature and salinity respectively, for each of the points along the bifurcation diagram. Each grid point represents a node in the network. The basin that we have used here contains 16 grid points in the vertical direction and 32 points in the latitudinal direction, so the highest possible degree is 511.

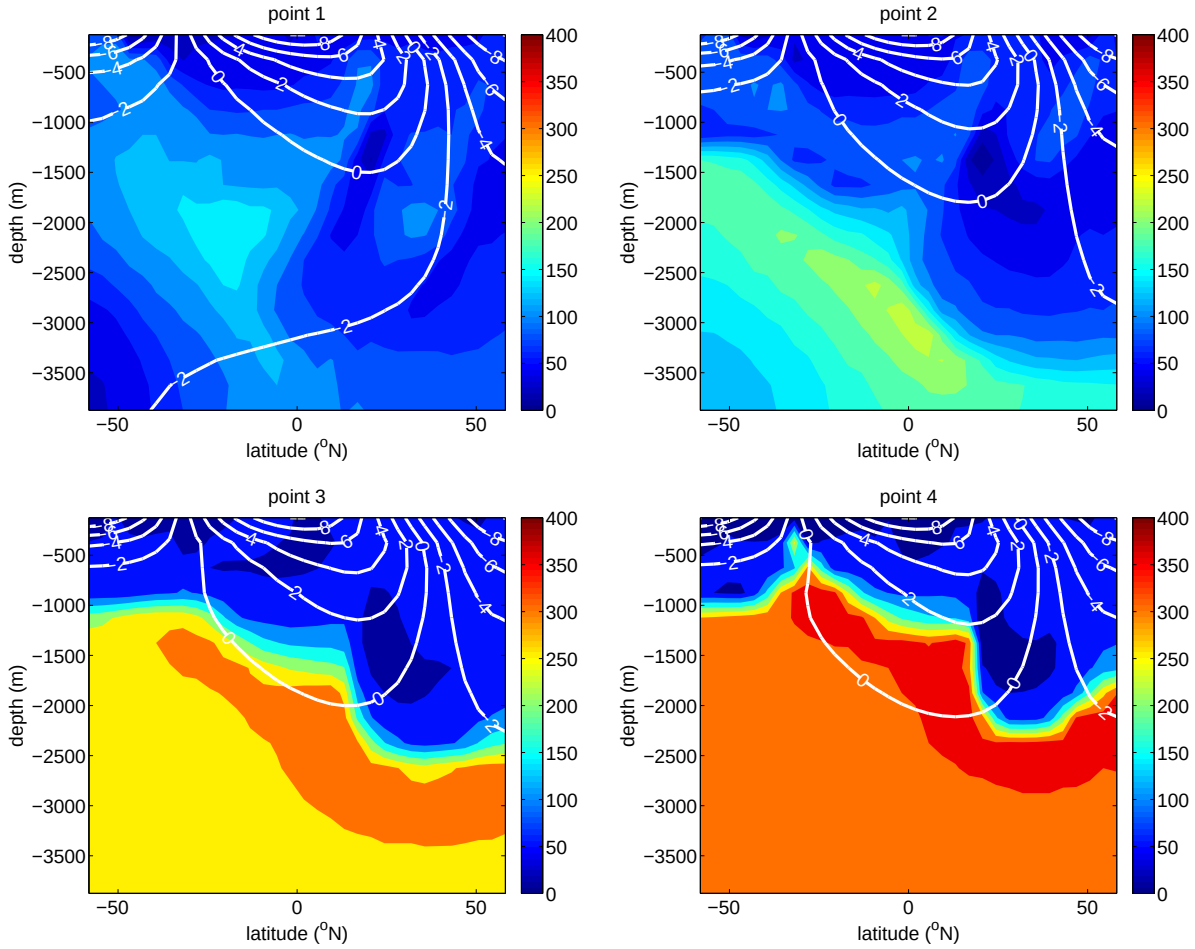

Figure 4.3: Degree of the temperature network, constructed using a threshold value $\tau = 0.7$, shown at each of the four points when approaching the tipping point. Contour lines of the steady state temperature are plotted in white.

In case of the temperature, we see that a clear change occurs when approaching the tipping point. In the lower part of the basin, the degree increases until the network becomes almost fully connected. In point 4, closest to the tipping point, the degree has increased in the largest portion of the basin, with the exception of the upper layer. At a depth of approximately 1000 m, there is a clear transition between high degree in the lower basin and low degree in the upper layer. Also, from about 15°N to 60°N, a dip in the transition line can be seen. At around -30°N a small rise is present.

In the salinity network, the degree also generally increases when approaching the tipping point. The clear boundary between the lower layers with high degree and the upper layers with low degree is also present in the salinity network. However, in case of the salinity the transition line is at a deeper level, so a larger part of the basin consists of nodes with a low degree. Because of this the dip at 15°N to 60°N is less pronounced than in the case of the temperature. Another difference is the maximum degree, which is around 250 for the salinity network compared to about 350 for the temperature network.

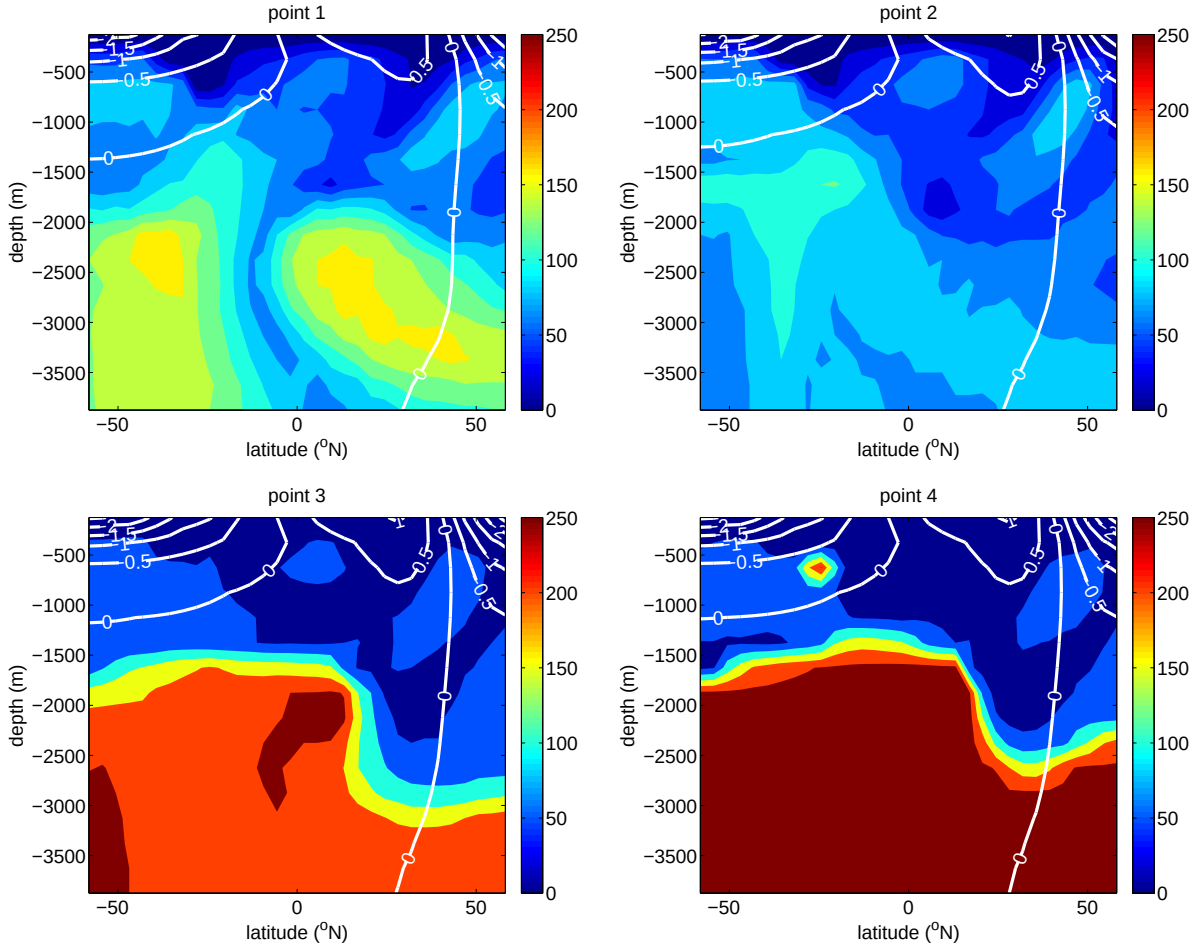

Figure 4.4: Degree of the salinity network, constructed using threshold value $\tau = 0.7$, shown at each of the four points when approaching the tipping point. Contour lines of the steady state salinity are plotted in white.

So, in both figures 4.3 and 4.4 we see a clear evolution of the network degree, most notably the degree in the lower part of the basin increases. The change becomes even more apparent when the degree distribution is presented, as can be seen in figure 4.5 for the temperature and figure 4.6 for the salinity. In point 1 one broad peak is present, in point 2 the peaks seem to separate from each other and in points 3 and 4 we clearly see two separate narrow peaks. The peak on the right becomes quite narrow in point 4 and also increases in height.

We have also constructed networks for longer temperature and salinity time series, of 2000 years instead of 500 years, and with threshold values $\tau = 0.6$ and $\tau = 0.8$. The results are similar and are shown in the appendix.

We will now attempt to explain the change in network topology by considering the eigenvectors and empirical orthogonal functions (EOFs) of the model system.

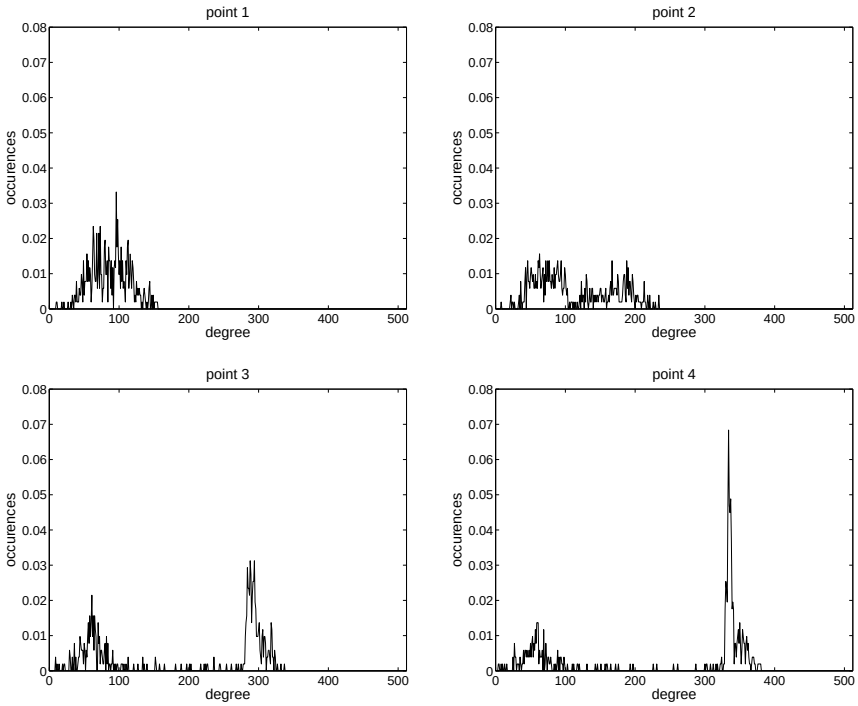

Figure 4.5: Degree distribution of the temperature network in each of the four points approaching the tipping point. On the horizontal axis the degree is shown, on the vertical axis the occurrence of a particular degree.

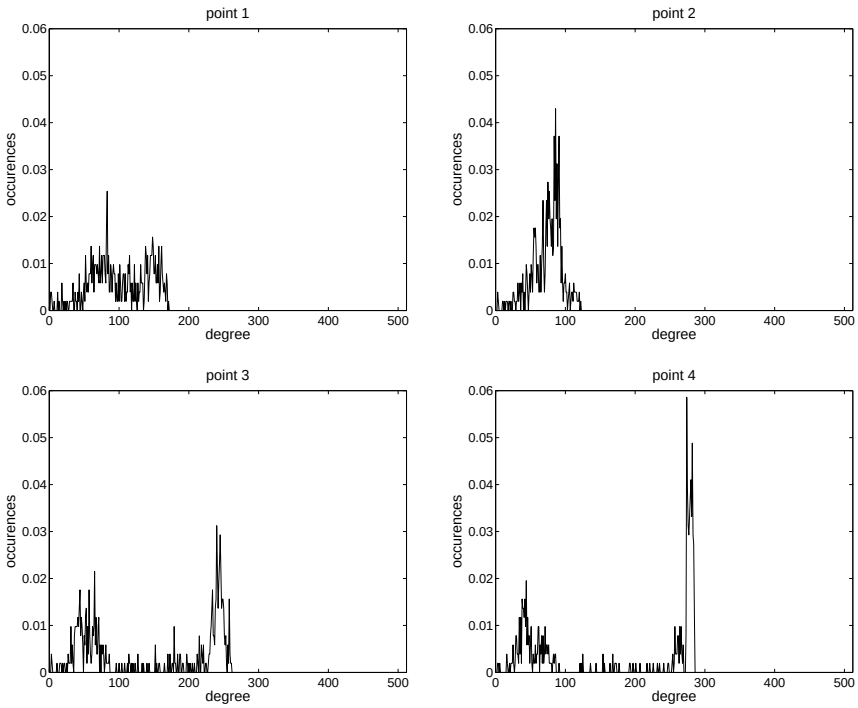

Figure 4.6: Degree distribution of the salinity network in each of the four points approaching the tipping point. On the horizontal axis the degree is shown, on the vertical axis the occurrence of a particular degree.

4.3 Eigenvectors

In chapter 2 we saw that a saddle-node bifurcation takes place when a real eigenvalue σ_r of the linear stability problem crosses the imaginary axis. Before the tipping point the steady solutions are stable and so $\sigma_r < 0$. Upon passing the bifurcation however, $\sigma_r > 0$ and perturbations will grow and the solution becomes unstable. Since the real eigenvalue is of importance in the tipping point, it is interesting to see whether we can find such an eigenvalue and the corresponding eigenvectors and follow its evolution through all of the four points.

The eigenvectors of the temperature and salinity in the points 1 and 4 are shown in figures 4.7 and 4.8, with the corresponding eigenvalues indicated below the figures.

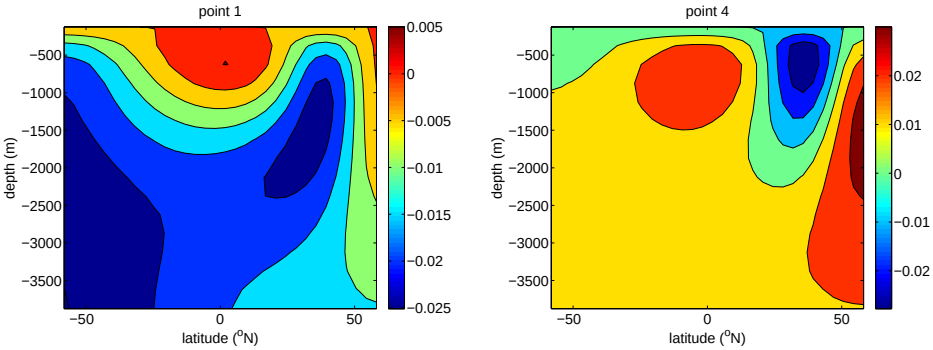

(a) $\sigma_r = -0.31 \times 10^{-2}$ (b) $\sigma_r = +0.13 \times 10^{-2}$

Figure 4.7: Temperature field at the dominant eigenmode, in point 1 and point 4. Note the different colour scale of the figures. Eigenvalues are indicated below each figure.

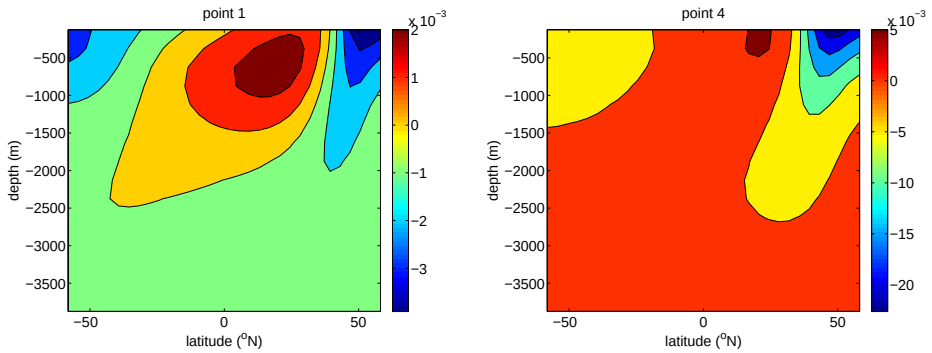

(a) $\sigma_r = -0.31 \times 10^{-2}$ (b) $\sigma_r = +0.13 \times 10^{-2}$

Figure 4.8: Salinity field of the dominant eigenmode, in point 1 and point 4. Note the different colour scale of the figures. Eigenvalues are indicated below each figure.

In case of the temperature, it is interesting to see that the eigenvector in point 4 has the same general shape as the degree in figure 4.3. The same dip in the northern hemisphere, and a small rise in the southern hemisphere can be seen.

Although in the salinity case the shape of the eigenvectors is a lot less clear than those of the temperature, the shape of the eigenvector in point 4 is similar to the dip seen in the network degree.

4.4 Empirical Orthogonal Functions (EOFs)

The data can be decomposed into spatial empirical orthogonal functions (EOFs) and the time series of the principal components (PCs). Here, we compute the EOFs for the data sets at each of the four points approaching the tipping point, using the covariance matrix to set up the eigenvalue problem from which the EOFs are solved.

Suppose that our data set is again represented by the matrix F, ordered so that each column contains the time series of a grid point. We then form the covariance matrix R by calculating

$$R = F^T F,$$

where the superscript T indicates the transpose. Next, we solve the eigenvalue problem

$$RC = C\Lambda,$$

where Λ is a diagonal matrix containing the eigenvalues λ_i of R. The eigenvectors of R corresponding to the eigenvalues λ_i are the column vectors $\mathbf{c}_i$ of the matrix C. These eigenvectors $\mathbf{c}$ are the EOFs that we are looking for. The 'importance' of EOF_i can be found by dividing λ_i by the sum of all the other eigenvalues. This then gives the fraction of the total variance in R that is explained by an EOF.

Now that we have found the EOFs, the principal component time series of the EOFs can be found by calculating

$$\mathbf{a}_i = F\mathbf{c}_i,$$

where the vector $\mathbf{a}_i$ represents the PC corresponding to the EOF $\mathbf{c}_i$.

The data can also be reconstructed from the EOFs and PCs by

$$F = \sum_{j=1}^{N} \mathbf{a}_j \mathbf{c}_j^T, \tag{4.1}$$

where N is the number of grid points.

We compute the EOFs of the temperature and find that the first three EOFs account for about 90% of the variability. In figures 4.9 to 4.11 these EOFs are shown. In case of the salinity, the first three EOFs account for about 80% of the variance. The EOFs of the salinity are shown in figures 4.12 to 4.13, the percentage of the variance that each EOF explains is indicated below each figure.

It is interesting to see that from point 1 up to point 3 the first two EOFs of the temperature decrease in importance, while the third increases. In point 4 however, EOF1 increases from roughly 45% to 60%, EOF2 decreases from about 30% to 20% and EOF3 from 17% to 13%. Apparently, EOF1 becomes more dominant upon approaching the tipping point.

In case of the salinity however, EOF1 continues to decrease in importance, while EOF2 and EOF3 increase. In terms of the patterns of the EOFs, they do not change a lot from point to point and they do not show a clear resemblence to the network degree in figure 4.4.

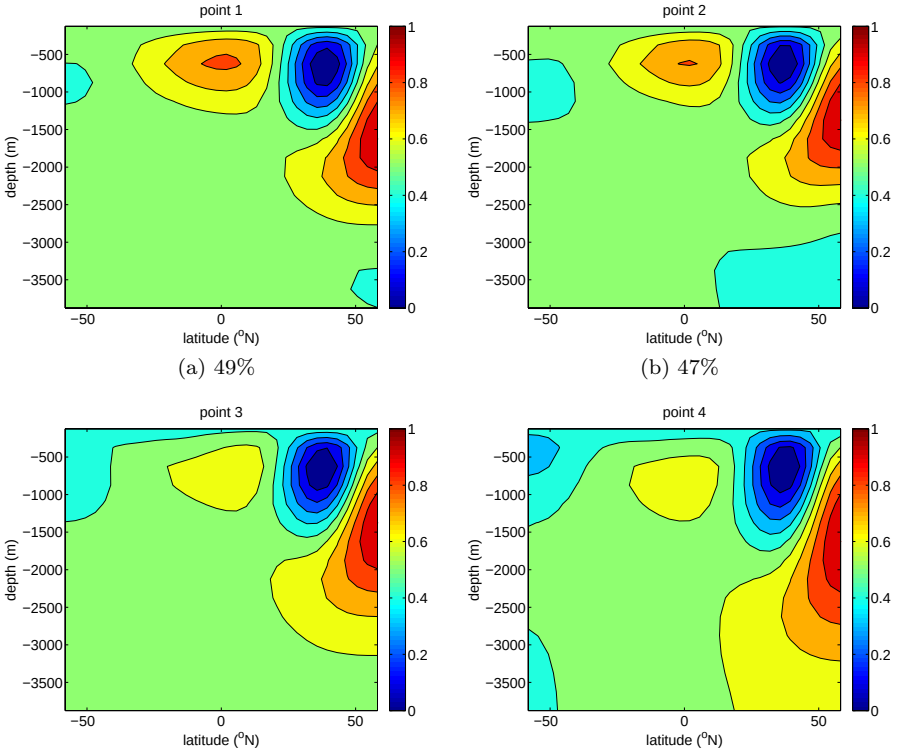

(a) 49% (b) 47%

(c) 45% (d) 60%

Figure 4.9: Pattern of the first EOF of the temperature field at each of the four points approaching the tipping point. The percentage of the variance that is explained by EOF1 is indicated below each figure.

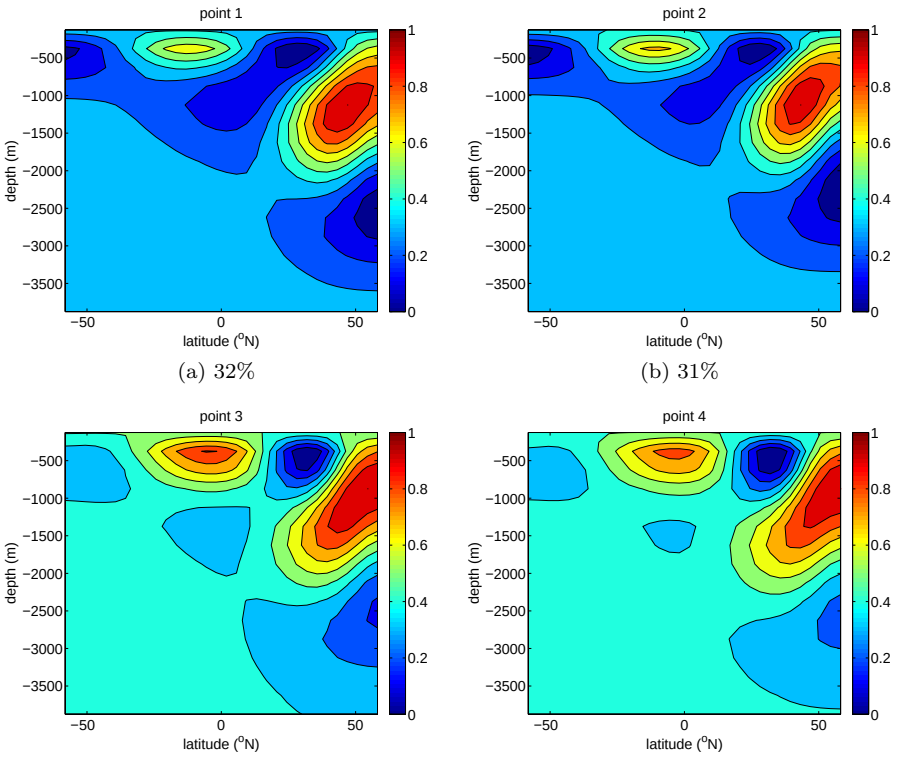

(a) 32% (b) 31%

(c) 29% (d) 21%

Figure 4.10: Pattern of the second EOF of the temperature field at each of the four points approaching the tipping point. The percentage of the variance that is explained by EOF2 is indicated below each figure.

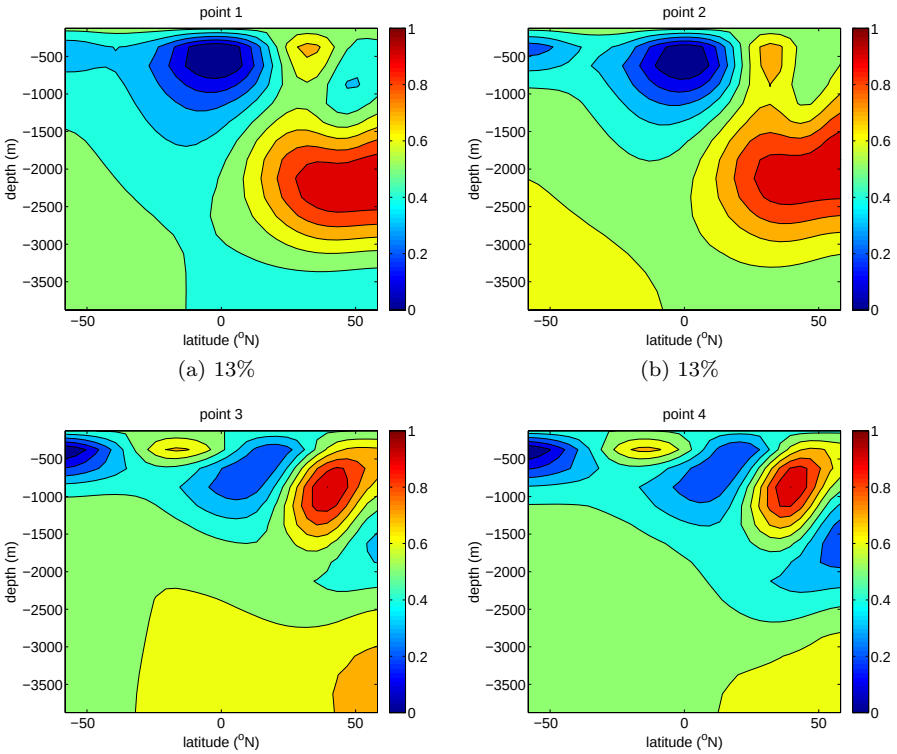

(a) 13% (b) 13%

(c) 17% (d) 13%

Figure 4.11: Pattern of the third EOF of the temperature field at each of the four points approaching the tipping point. The percentage of the variance that is explained by EOF3 is indicated below each figure.

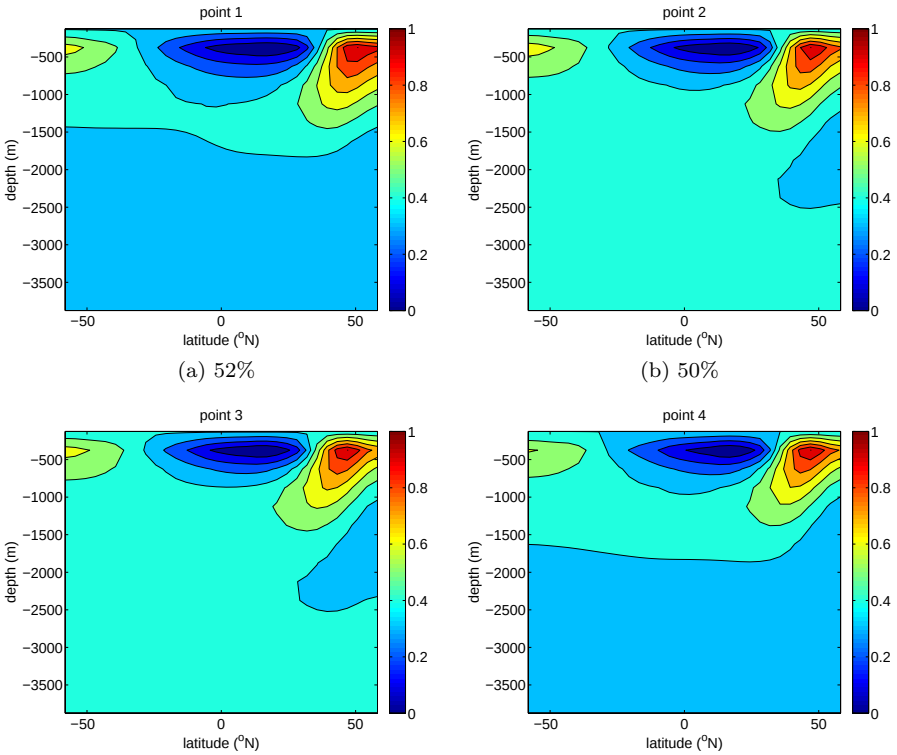

(a) 52% (b) 50%

(c) 46% (d) 45%

Figure 4.12: Pattern of the first EOF of the salinity field at each of the four points approaching the tipping point. The percentage of the variance that is explained by EOF1 is indicated below each figure.

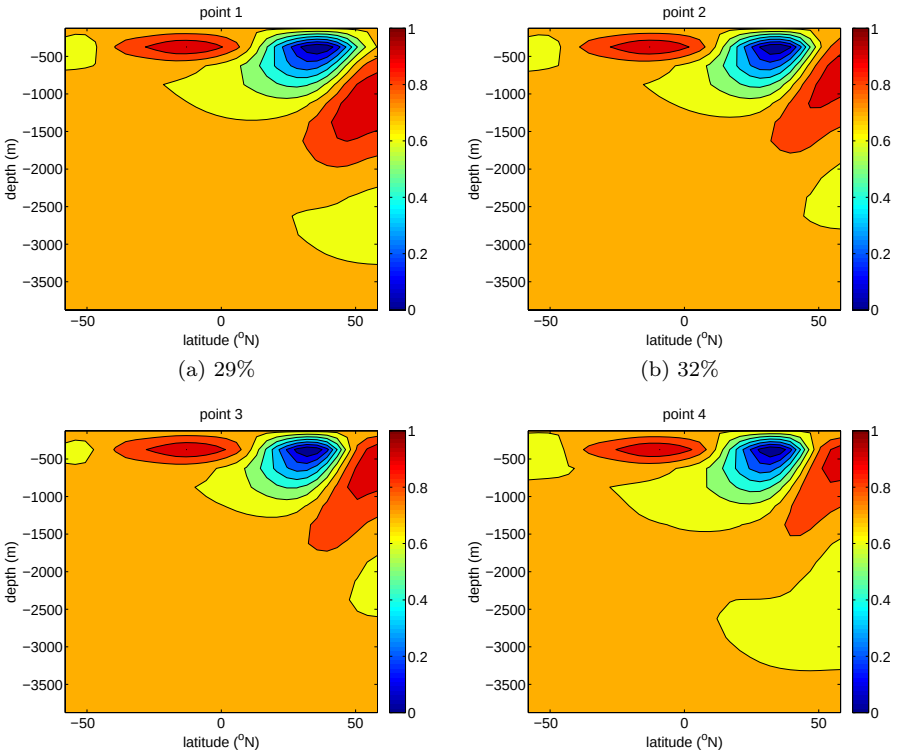

(a) 29% (b) 32%

(c) 34% (d) 33%

Figure 4.13: Pattern of the second EOF of the salinity field at each of the four points approaching the tipping point. The percentage of the variance that is explained by EOF2 is indicated below each figure.

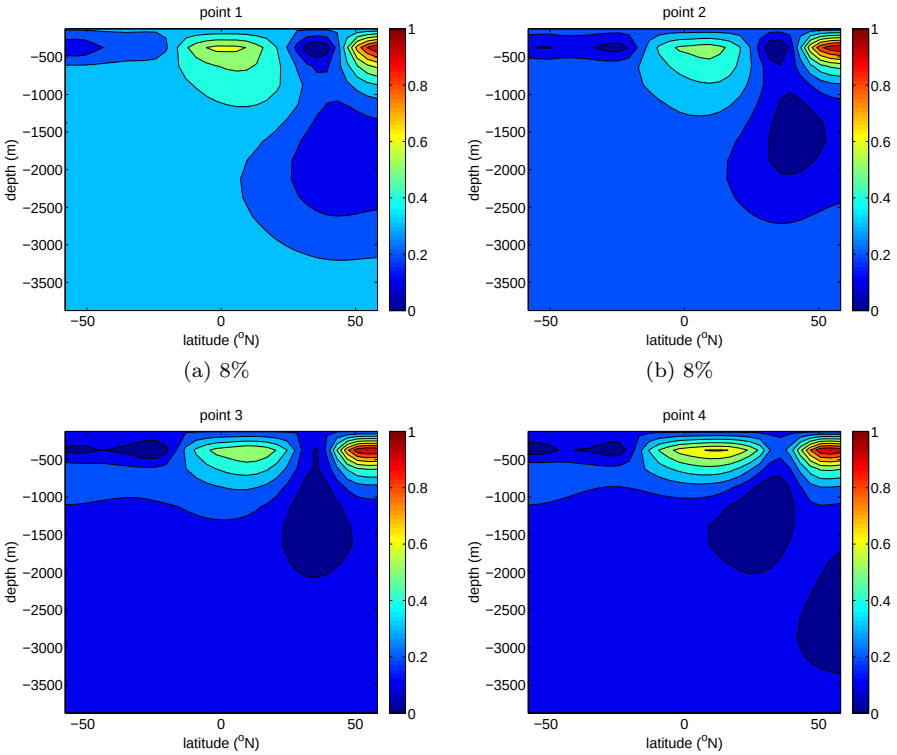

(a) 8% (b) 8%

(c) 9% (d) 11%

Figure 4.14: Pattern of the third EOF of the salinity field at each of the four points approaching the tipping point. The percentage of the variance that is explained by EOF3 is indicated below each figure.

4.4.1 Reconstructed networks

We would now like to know how these EOFs influence the network. We partly reconstruct the data from the first three EOFs by using equation 4.1. In this way we get

$$\begin{aligned} F_1 &= \mathbf{a}_1\mathbf{c}_1^T, \\ F_2 &= \mathbf{a}_1\mathbf{c}_1^T + \mathbf{a}_2\mathbf{c}_2^T, \\ F_3 &= \mathbf{a}_1\mathbf{c}_1^T + \mathbf{a}_2\mathbf{c}_2^T + \mathbf{a}_3\mathbf{c}_3^T, \end{aligned}$$

From F_1, F_2 and F_3 we can create networks and investigate their influence on the total network. As mentioned in chapter 3, the linear Pearson correlation coefficient is used. In terms of the data matrix F, the correlation matrix r can be written as

$$r_{ij} = \frac{(F^TF)_{ij}}{\sqrt{(F^TF)_{ii}(F^TF)_{jj}}},$$

where the subscripts ij indicate the element of a matrix on the ith column and the jth row.

Consider the correlation matrix of $F_1 = \mathbf{a}_1\mathbf{c}_1^T$,

$$r_{ij} = \frac{(\mathbf{c}_1\mathbf{a}_1^T\mathbf{a}_1\mathbf{c}_1^T)_{ij}}{\sqrt{(\mathbf{c}_1\mathbf{a}_1^T\mathbf{a}_1\mathbf{c}_1^T)_{ii}(\mathbf{c}_1\mathbf{a}_1^T\mathbf{a}_1\mathbf{c}_1^T)_{jj}}},$$

$\mathbf{a}_1^T\mathbf{a}_1$ returns a number so this can be written as

$$r_{ij} = \frac{\mathbf{a}_1^T\mathbf{a}_1(\mathbf{c}_1\mathbf{c}_1^T)_{ij}}{\sqrt{(\mathbf{a}_1^T\mathbf{a}_1)^2(\mathbf{c}_1\mathbf{c}_1^T)_{ii}(\mathbf{c}_1\mathbf{c}_1^T)_{jj}}} = \frac{\mathbf{a}_1^T\mathbf{a}_1(\mathbf{c}_1\mathbf{c}_1^T)_{ij}}{\sqrt{(\mathbf{a}_1^T\mathbf{a}_1)^2(\mathbf{c}_1\mathbf{c}_1^T)_{ij}^2}} = 1.$$

From this it follows that a network constructed only from the first EOF is a fully connected network since all correlations are 1.

However, the networks constructed from F_2 and F_3 are not fully connected, since the correlation coefficient contains crossterms. The degree of the networks of F_2 and F_3 in all four points are plotted in figures 4.15 and 4.16 for the temperature and in figures 4.17 and 4.18 for the salinity.

In case of the temperature, both the networks constructed from F_2 and from F_3 show a development in the degree when approaching the tipping point that is similar to what we observed in figure 4.3. In both cases, the degree in the lower layers increases and in point 4 there is a clear transition. The dip and the rise in point 4 that we saw in figure 4.3 are also visible in figures 4.15 and 4.16. However, in case of the network constructed from F_2, there are some small islands of high degree present in the areas of low degree. Furthermore, the degree in general and in the lower layers specifically is much higher than in the network from the original data. When including the third EOF in the network constructed from F_3, the islands of high degree disappear and the degree is smaller. The network constructed from F_3 resembles that from the original data very closely.

In general we can say that upon approaching the tipping point, the degree increases in the lower part of the basin. We also saw that EOF1 becomes more dominant and that the network of F_1 is fully connected.

In case of the salinity, the network constructed from F_2 shows entirely different results. This network shows little resemblance to the network from the original data. With a lot of imagination the patterns seen in figure 4.17 can also be seen in figure 4.4, but in figure 4.17 it is too pronounced and the degree is too high. The network constructed from F_3 is much more promising. The patterns seen here are similar to the original network and the degree is lower than in the F_2 network. Apparently, in case of the salinity it is much more important to include the third EOF than it is for the temperature.

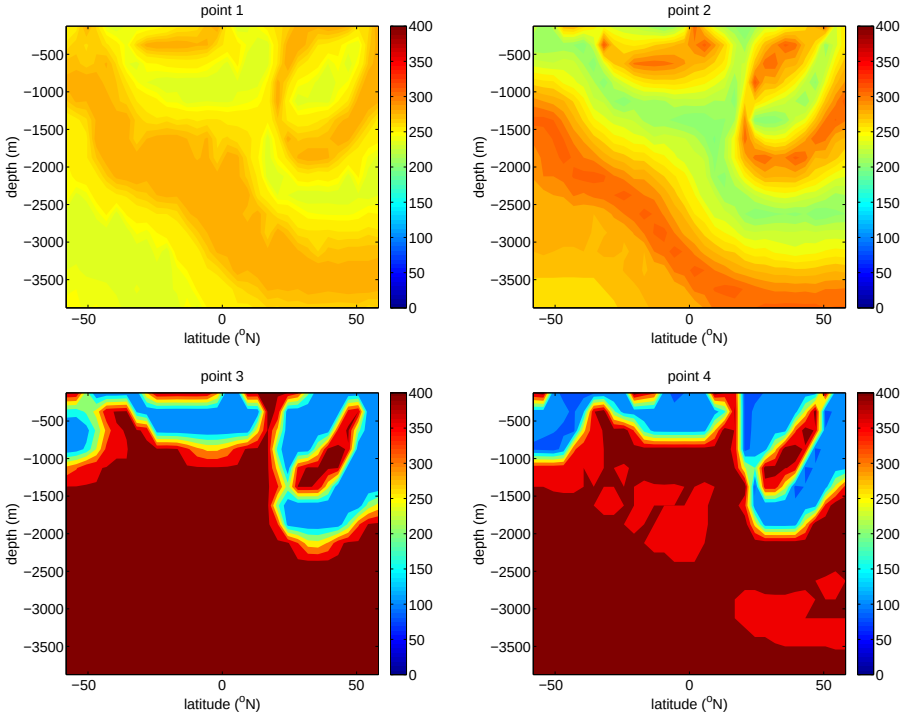

Figure 4.15: Degree of the network constructed from F_2, consisting of EOF1 and EOF2 of the temperature, with threshold value $\tau = 0.7$, shown at each of the four points approaching the tipping point.

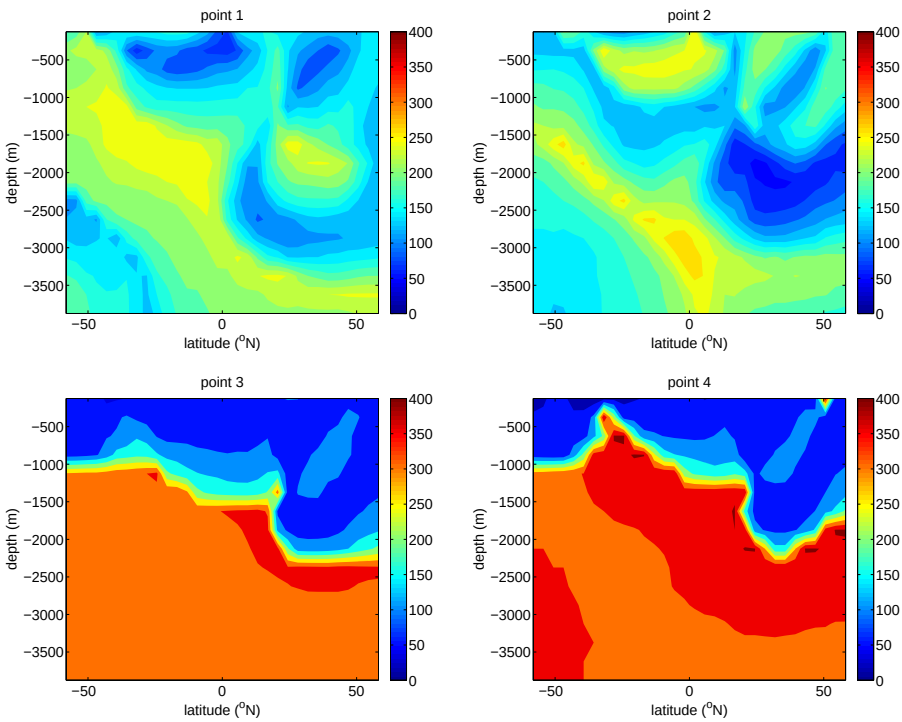

Figure 4.16: Degree of the network constructed from F_3, consisting of EOF1, EOF2 and EOF3 of the temperature, with threshold value $\tau = 0.7$, shown at each of the four points approaching the tipping point.

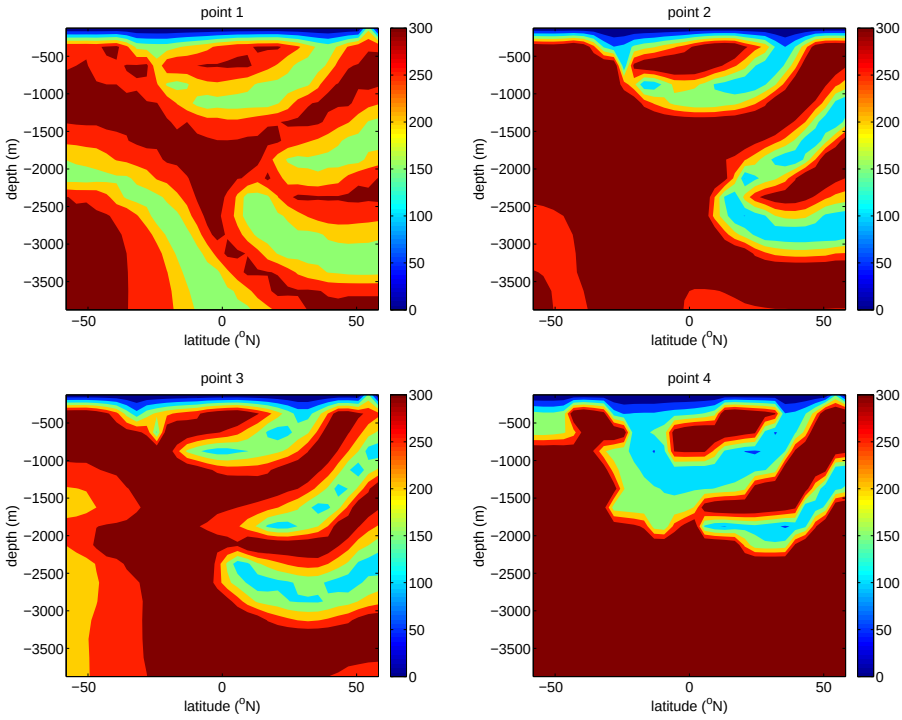

Figure 4.17: Degree of the network constructed from F_2, consisting of EOF1 and EOF2 of the salinity, with threshold value $\tau = 0.7$, shown at each of the four point approaching the tipping point.

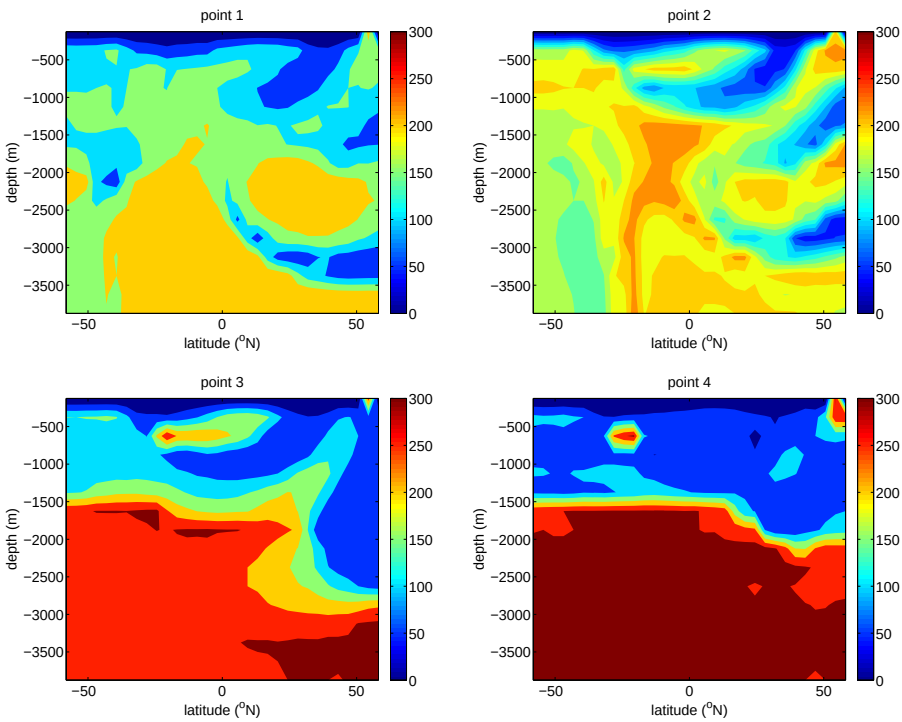

Figure 4.18: Degree of the network constructed from F_3, consisting of EOF1, EOF2 and EOF3 of the salinity, with threshold value $\tau = 0.7$, shown at each of the four points approaching the tipping point.

4.4.2 Correlation EOFs

To gain more insight into the topology of the network degree, we can also construct EOFs using the linear Pearson correlation matrix r. In contrast to the EOFs that are normally used, these EOFs account for a percentage of the correlation, rather than the variance. We have again constructed the first three EOFs, which account for about 80 to 90% in the temperature case and 80% in the salinity case. EOFs for the temperature are shown in figures 4.19 to 4.21 and in figures 4.22 to 4.24 for the salinity.

The first correlation EOF of the temperature clearly has the same shape as the network degree in figure 4.3. Also, EOF1 steadily increases in importance when approaching the tipping point, while EOF2 and EOF3 decrease.

In case of the salinity, EOF1 does become more dominant upon approaching the tipping point and the importance of EOF2 and EOF3 decreases. The shape of EOF1 also resembles the shape of the network degree of the original data.

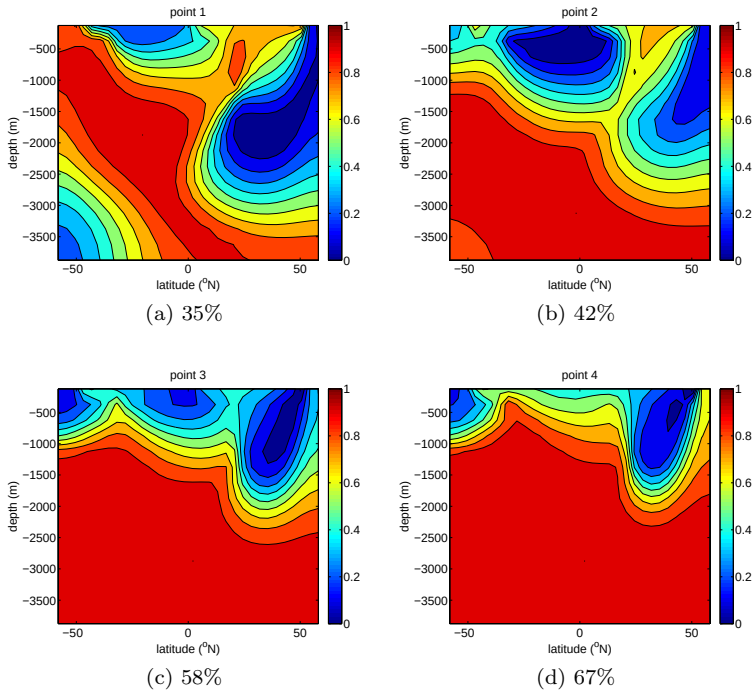

(a) 35% (b) 42%

(c) 58% (d) 67%

Figure 4.19: Pattern of the first correlation EOF of the temperature field at each of the four points approaching the tipping point. The percentage of the variance that is explained by EOF1 is indicated below each figure.

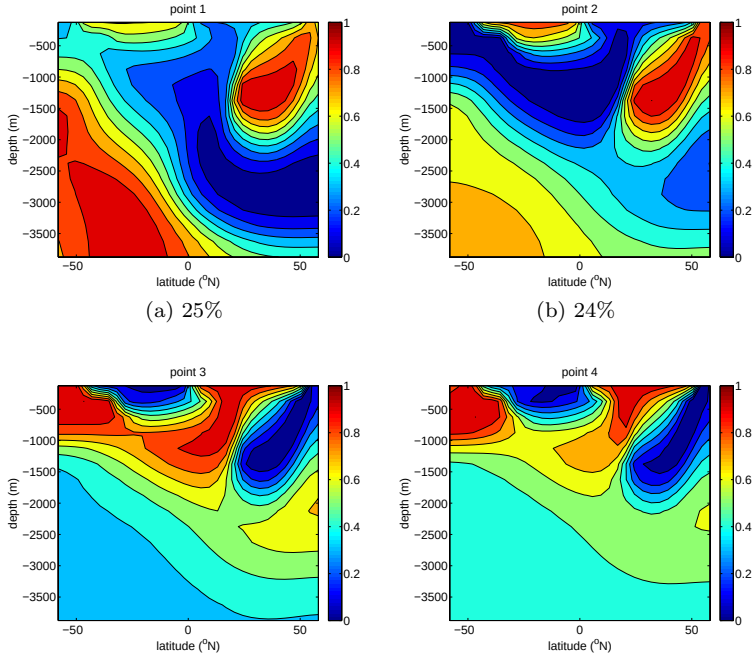

(a) 25% (b) 24%

(c) 17% (d) 15%

Figure 4.20: Pattern of the second correlation EOF of the temperature field at each of the four points approaching the tipping point. The percentage of the variance that is explained by EOF2 is indicated below each figure.

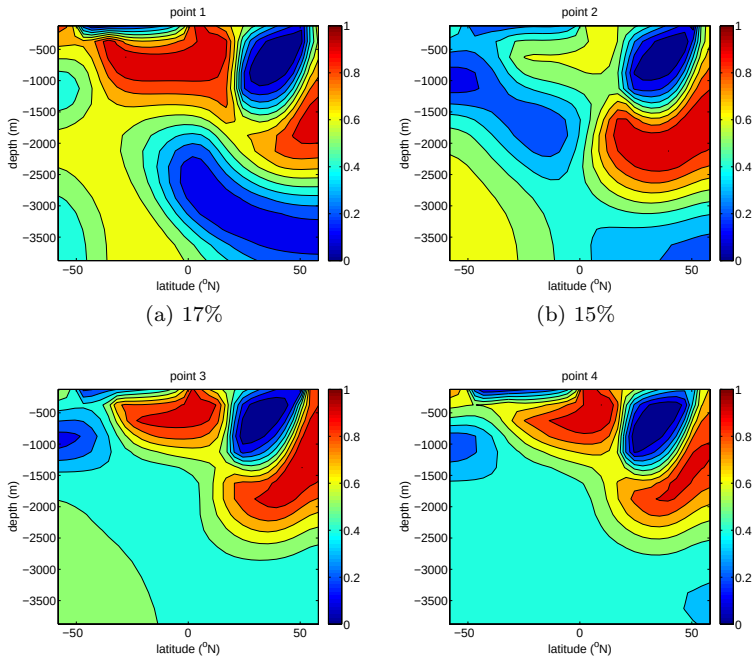

(a) 17% (b) 15%

(c) 14% (d) 11%

Figure 4.21: Pattern of the third correlation EOF of the temperature field at each of the four points approaching the tipping point. The percentage of the variance that is explained by EOF3 is indicated below each figure.

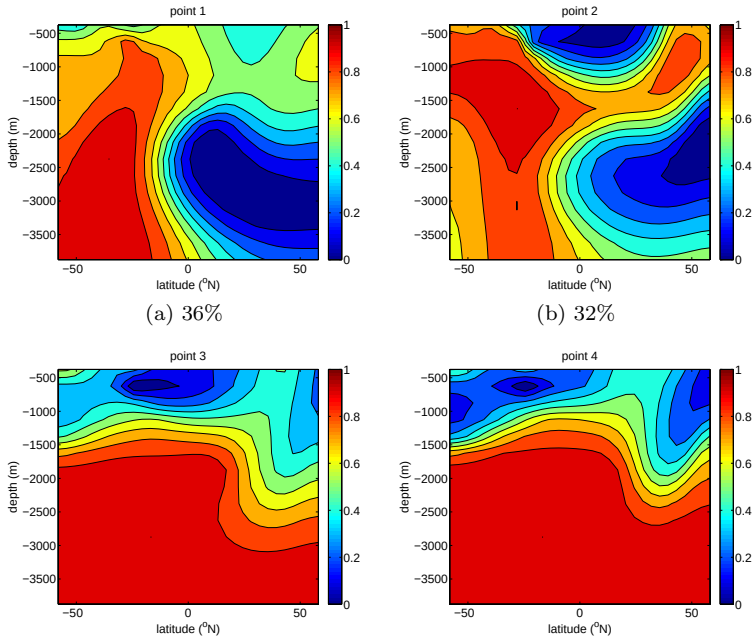

(a) 36% (b) 32%

(c) 51% (d) 59%

Figure 4.22: Pattern of the first correlation EOF of the salinity field at each of the four points approaching the tipping point. The percentage of the variance that is explained by EOF1 is indicated below each figure.

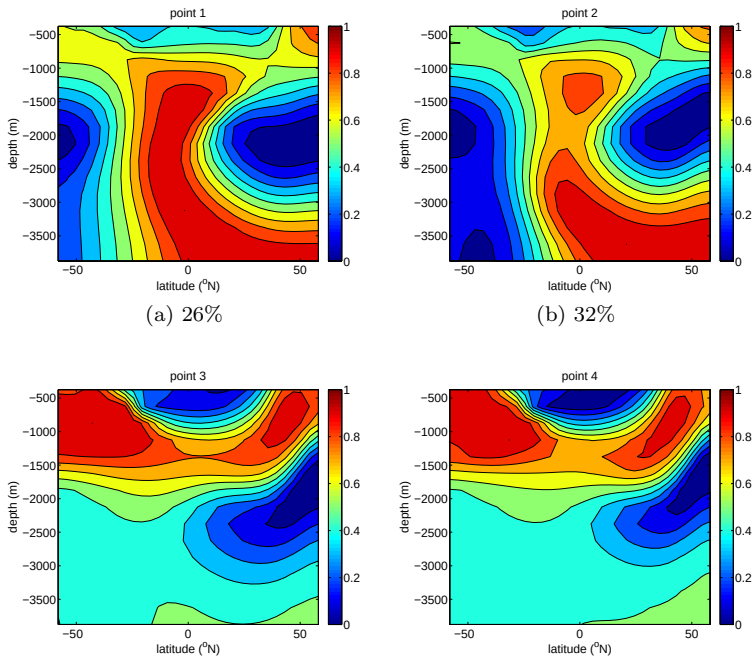

(a) 26% (b) 32%

(c) 21% (d) 19%

Figure 4.23: Pattern of the second correlation EOF of the salinity field at each of the four points approaching the tipping point. The percentage of the variance that is explained by EOF2 is indicated below each figure.

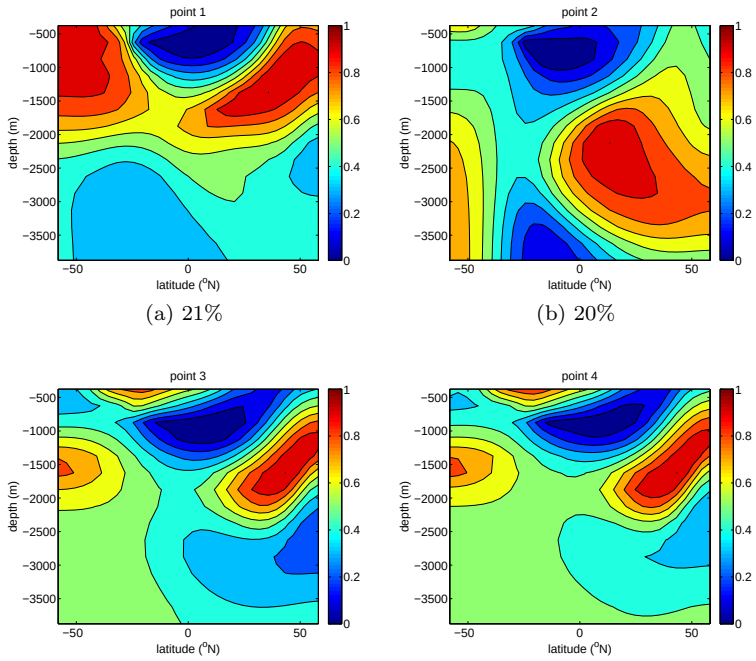

(a) 21%

(b) 20%

(c) 13%

(d) 12%

Figure 4.24: Pattern of the third correlation EOF of the salinity field at each of the four points approaching the tipping point. The percentage of the variance that is explained by EOF3 is indicated below each figure.

4.5 Limited grid networks

Ideally, we would like to construct networks from oceanographic data and find an indicator for the tipping point of the MOC from these networks. However, the resolution of this data is limited. Because of this, we want to know whether networks constructed from lower spatial resolution grids also show a warning signal. Therefore we create networks from two different grids with fewer nodes and at different locations. The first grid contains 32 grid points at the surface and 32 points at the bottom of the basin, we refer to this as the depth-surface grid. The second grid has 16 points in the north and south of the basin, which cover the entire depth of the basin. This grid is referred to as the north-south grid. These grids are shown in figure 4.25 for clarity.

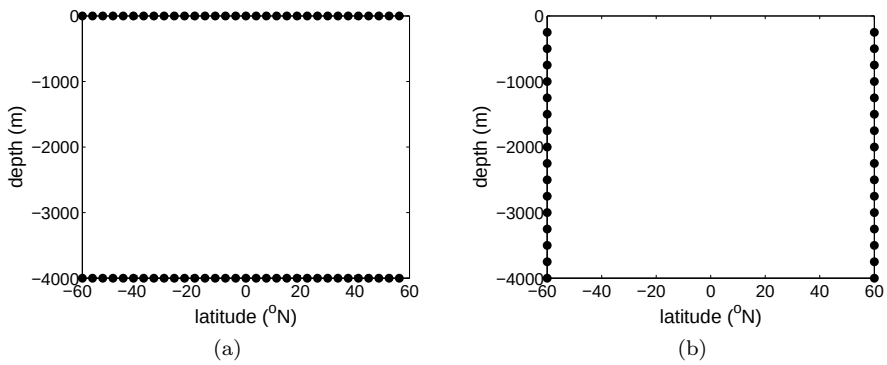

Figure 4.25: (a) Depth-surface grid. In total 64 grid points, with 32 points at the bottom of the basin and at the surface. (b) North-south grid. In total 32 points, with 16 points at both the northern and southern edge of the basin.

Using these grids, we once again construct networks at each of the four points approaching the tipping point. The degree of the networks constructed from the temperature are shown in figures 4.26 and 4.27.

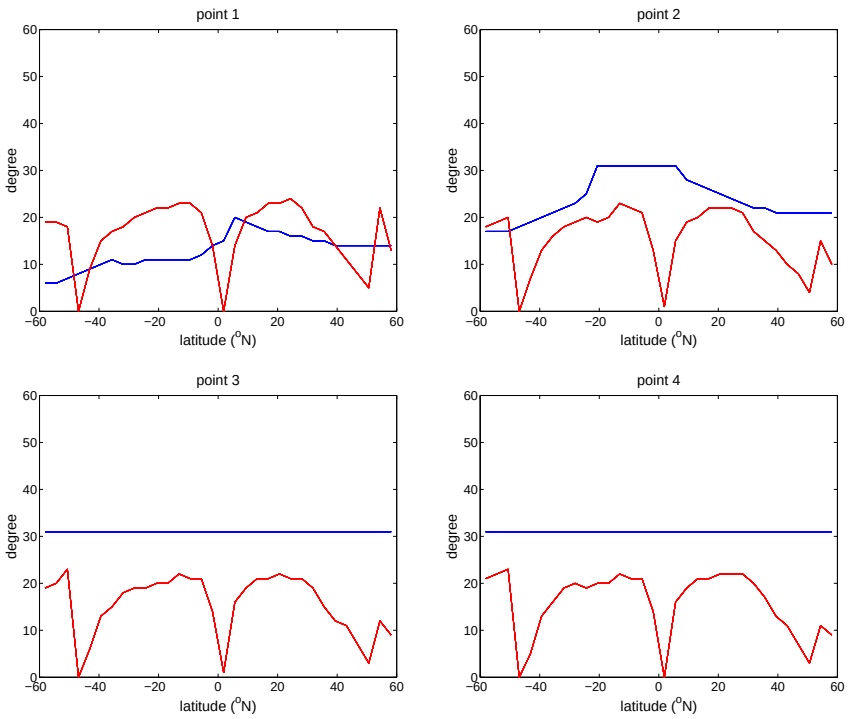

Figure 4.26: Degree constructed from the temperature. Depth-surface grid shown in figure 4.25a has been used. The blue line shows the degree of the bottom of the basin, red that of the surface.

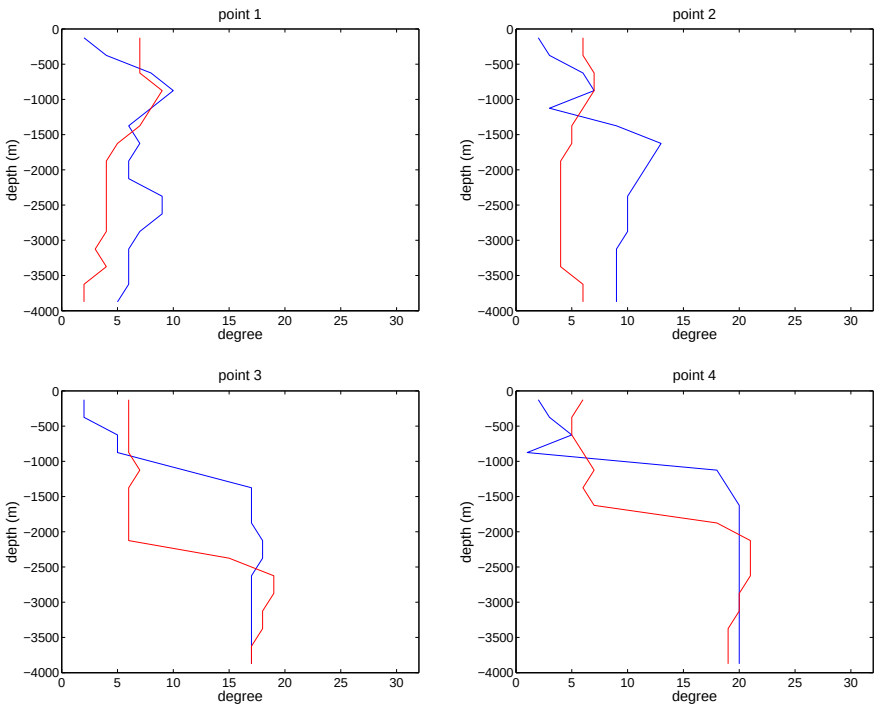

Figure 4.27: Degree constructed from the temperature. North-south grid from figure 4.25b has been used. The blue line shows the degree of the nodes in the south, the red line the degree of nodes in the north. Note that the degree is plotted on the horizontal axis and the depth on the vertical axis.

The degree of the depth-surface grid in figure 4.26 shows different behaviour in the depth and the surface, as was also the case for the original network in figure 4.3. The degree at the surface (red) does not show a clear evolution when approaching the tipping point, rather it appears to be latitude dependent. The degree at the bottom of the basin (blue) does show an evolution. As was the case for the original network, the bottom nodes become more connected.

The network constructed from the north-south grid in figure 4.27 also shows the same evolution as expected from the original network. In both the north (red) and south (blue), the degree increase in the lower part of the basin. In the south a higher degree is reached closer to the surface than in the north. This effect is also seen in figure 4.3.

As in section 4.2, we also consider the degree distribution, shown in figures 4.28 and 4.29.
In the degree distribution of the original temperature network (figure 4.5), we saw a separation of two peaks when approaching the tipping point and an increasing occurrence of higher degrees.

The degree distributions of the depth-surface and the north-south grids also show a peak of increasing height moving to the right when approaching the tipping point. A separation of the two peaks is also seen, though it is less pronounced in case of the depth-surface grid.

From the above figures, we can conclude that the evolution of the network is still visible when constructed from fewer nodes. However, the question is whether this evolution is enough to find an indicator that can provide a warning signal.

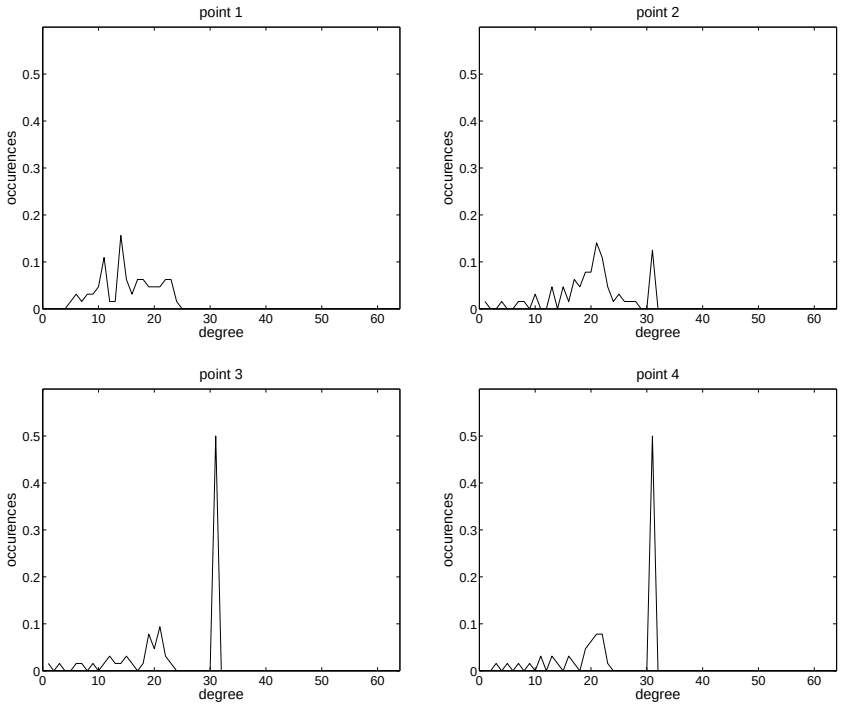

Figure 4.28: Degree distribution of the temperature network, constructed from the depth-surface grid in figure 4.25a.

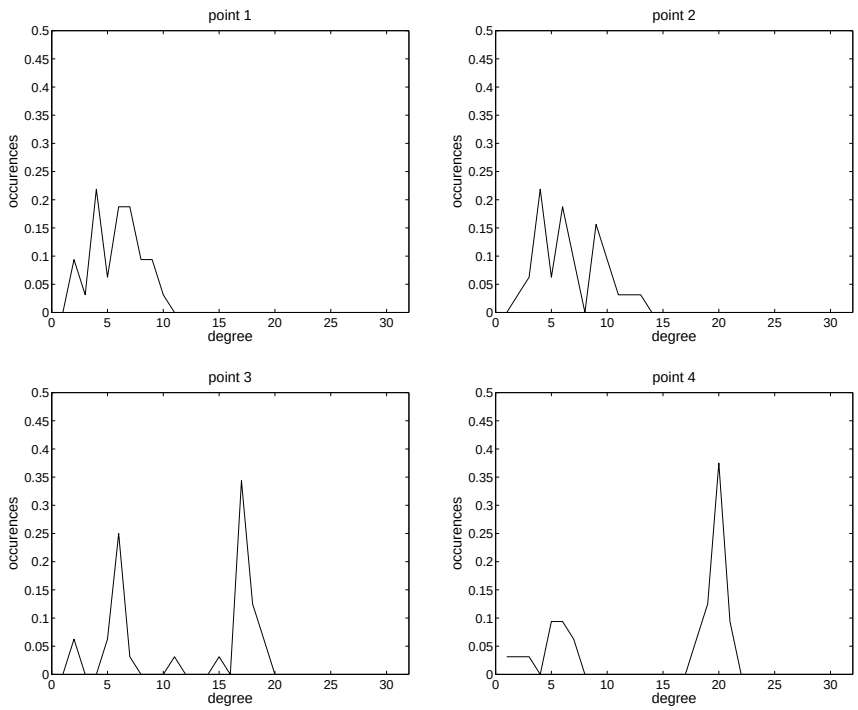

Figure 4.29: Degree distribution of the temperature network, constructed from the north-south grid in figure 4.25b.

4.6 Warning signal

We now want to define a possible indicator that can provide an early warning signal when approaching the tipping point of the MOC. In the degree distributions in figures 4.5, 4.6, 4.28 and 4.29 we saw a clear separation of two peaks and an increasing occurrence of higher degrees when approaching the tipping point. This clear evolution motivates us to use the degree ratio d_r as an indicator. The degree ratio is defined as

$$d_r = \frac{d}{d_{max}}, \tag{4.3}$$

where d is the highest value of the degree that is observed in the network and d_{max} is the degree of all nodes when the network is fully connected.

We compute this quantity at each of the four points indicated in the bifurcation diagram, as well as in four other intermediate points. We can then plot the degree ratio d_r as a function of the freshwater flux parameter β. In figure 4.30 this is plotted for the original temperature network as well as for the networks constructed from the depth-surface and north-south grids. Figure 4.31 shows the same for the salinity. As expected, the degree ratio increases when approaching the tipping point.

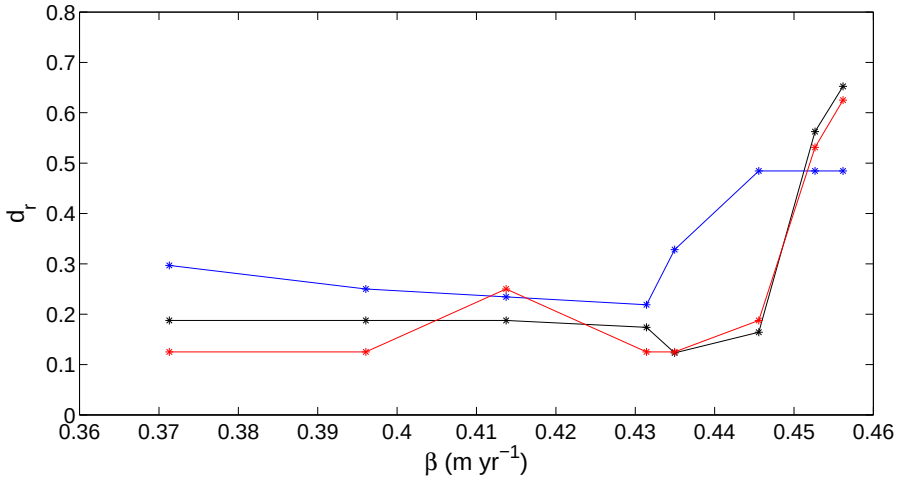

Figure 4.30: Degree ratio as a function of the freshwater flux parameter β, constructed from the original temperature network (black), the network from the depth-surface grid (blue) and from the north-south grid (red).

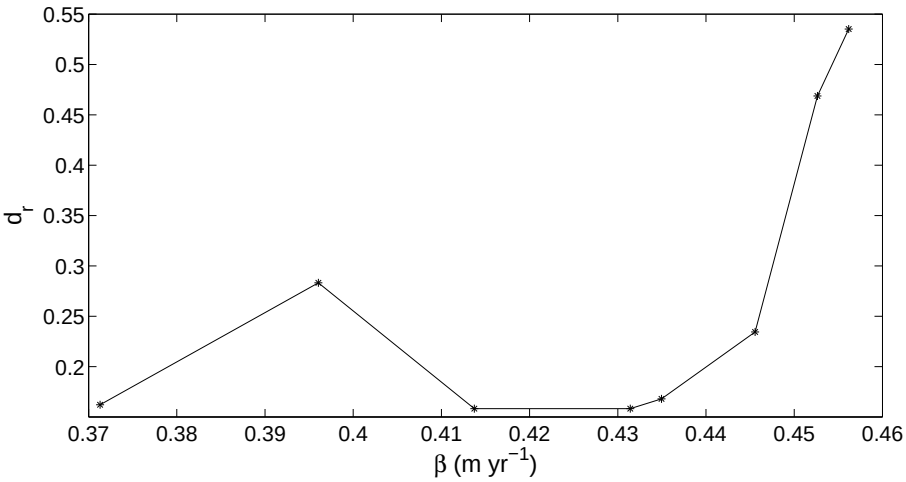

Figure 4.31: Degree ratio as a function of the freshwater parameter β, constructed from the salinity networks.

We can use the degree ratio to define an early warning signal in several different ways. The easiest way is by simply setting a threshold value for the degree ratio that signals the approaching tipping point. For example, we can define $d_r \geq 0.5$ to be the indicator for a warning signal. We see that in case of the original temperature and salinity networks, this threshold can indeed provide a warning. Especially for the temperature network an early warning is given, in case of the salinity network the warning is given later. The indicator is also sufficient for the limited north-south temperature grid. In case of the depth-surface grid however, no warning is received.

We can also define an indicator in different ways, for example by using the derivative or averages of the degree ratio. The derivative δ_d is found by calculating

$$\delta_d(k) = \frac{d_{r,k} - d_{r,k-1}}{\beta_k - \beta_{k-1}}.$$

A threshold value then needs to be set for the derivative to provide a warning.

When using averages, we can calculate the average ratio μ_r as

$$\mu_r(k) = \frac{\mu_k}{\mu_{k-1}},$$

for the kth degree ratio. In this way, we make use of previous records. When the average ratio reaches a certain threshold, a warning signal can be given.

Because we have only computed the degree ratio for eight different values of β, we find that both of these two methods cannot give us a good warning signal. Although more advanced measures also exist, setting a threshold $d_r \geq 0.5$ in most case provides us with an early warning signal that is sufficient for the scope of this thesis.

Chapter 5

Results: Asymmetrical forcing

In this chapter, we consider the asymmetrically forced MOC. We again construct the bifurcation diagram and create temperature networks at different points approaching the tipping point. EOFs are also investigated. We consider networks from limited grids and find an indicator for a warning signal.

5.1 Bifurcation diagram

The Meridional Overturning Circulation is now forced with an asymmetric freshwater flux, as described by equation 3.3. We can now find the multiple steady states of the system by varying the parameter β_n for a fixed value of $\beta = 0.34$ m yr^{-1}. The resulting bifurcation diagram is shown in figure 5.1. In this figure, the sum of the maximum Ψ_+ and minimum Ψ_- values of the strength of the MOC are plotted against the control parameter β_n.

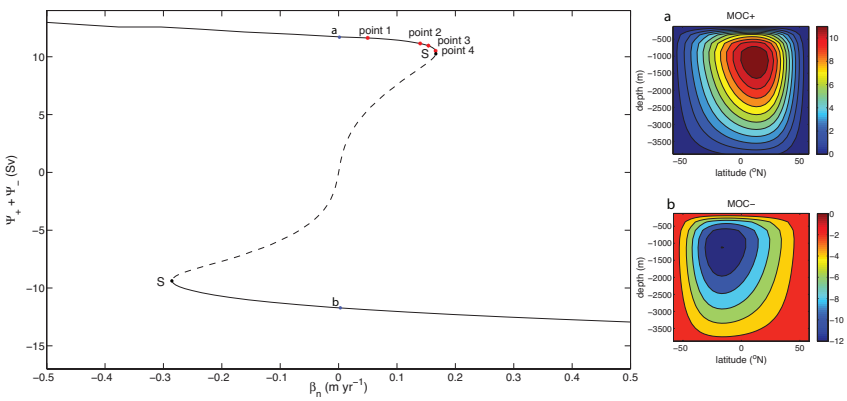

Figure 5.1: Left: Bifurcation diagram of the asymmetrically forced MOC. The sum of the maximum Ψ_+ and minimum Ψ_- values of the strength of the MOC are plotted against β_n. Stable steady solutions are indicated by drawn curves, unstable steady solutions by dashed curves. The points S indicate the saddle-node bifurcations. Points 1 to 4 are indicated for future reference. Right: Patterns of the MOC on both branches are shown. Locations where the examples were taken are indicated by the blue points labeled with a and b in the bifurcation diagram.

We see that the only two solutions are the asymmetrical MOC+ and MOC- states. Two saddle-node bifurcations (indicated with points S in the bifurcation diagram) are present and are connected by unstable steady states. For $\beta_n = 0$, both the stable MOC+ and MOC- solutions exist, as was also the case for symmetrical forcing (see figure **??**). The steady state MOC+ and MOC- solutions are shown in the left of figure 5.1.

As in chapter 4, four points that approach the tipping point S are indicated with stars in the bifurcation diagram. The coordinates of these points are given in table 5.1.

	β m yr^{-1}	$\Psi_+ - \Psi_-$(Sv)
point 1	0.0499	11.6
point 2	0.140	11.2
point 3	0.154	11.0
point 4	0.166	10.5

Table 5.1: Coordinates of the four points approaching the tipping point S indicated on the bifurcation diagram.

We again create a 500 year time series of the temperature at each of these four points by adding a reproducible random white noise perturbation to the forcing,

$$F_S = \beta \frac{\cos(\frac{\pi\theta}{\theta_N})}{\cos(\theta)} + \beta_n F_p(\theta) + \Delta w_r(\theta, t).$$

Again, w_r is the white noise perturbation that depends on latitude θ and time t and $Delta = 0.1$ is the amplitude of the perturbation. Using these time series, we can construct networks.

5.2 Networks

At each of the four points indicated in the bifurcation diagram, we construct networks from the temperature data, using a threshold value of $\tau = 0.7$. The degree of the temperature network at each of the four points is plotted in figure 5.2.

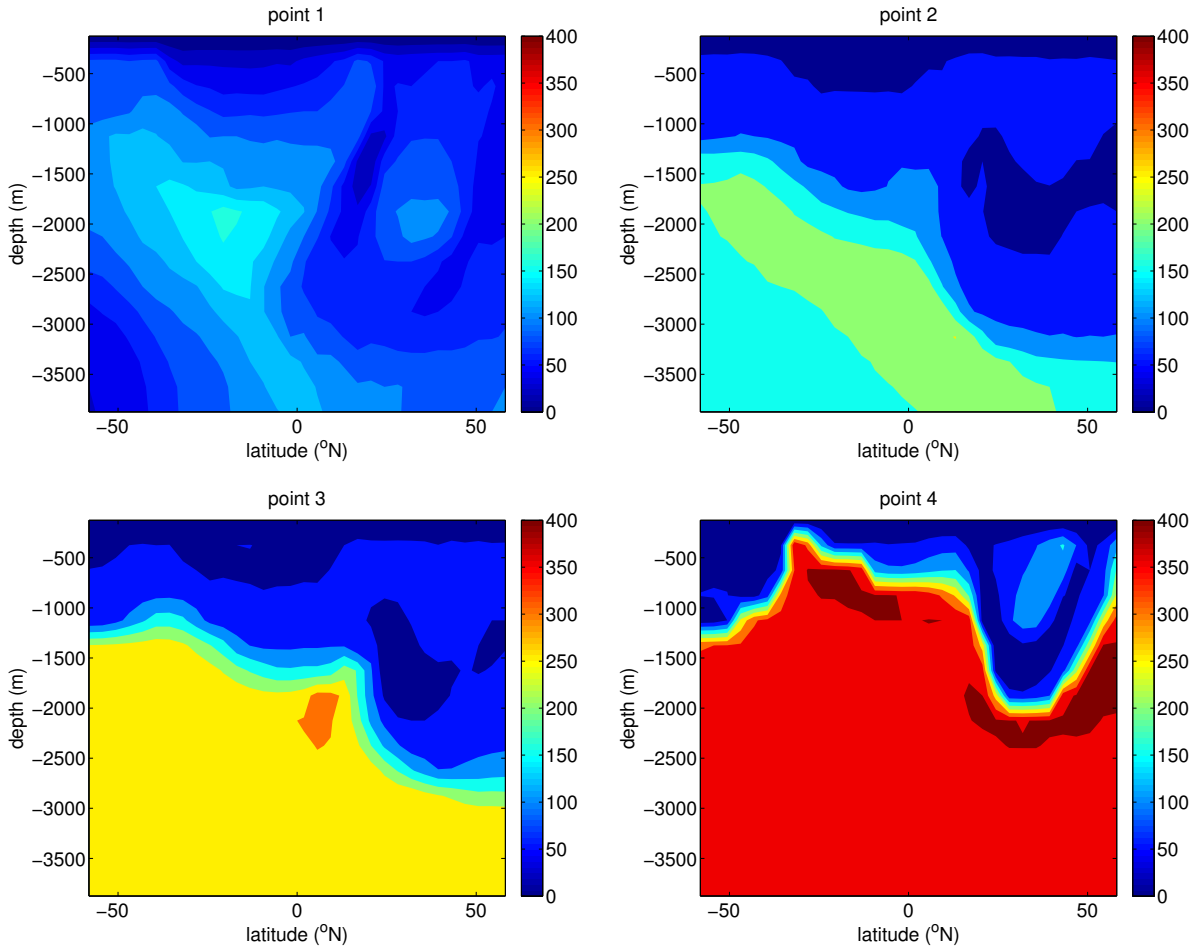

Figure 5.2: Degree of the temperature network, constructed with threshold value $\tau = 0.7$ at each of the four points approaching the tipping point.

The evolution of the network degree of the temperature is very similar to the case with symmetrical forcing in figure 4.3. We do see that the highest degree that is reached in this network is about 400, while in the symmetrical case it was 350.

We can also plot the degree distribution at each point along the bifurcation diagram. This is shown in figure 5.3. Here we again see that upon approaching the tipping point, two separate peaks in the degree distribution form. One peak moves further to the right and increases in height. To explain the evolution of the network degree, we again consider the EOFs of the system.

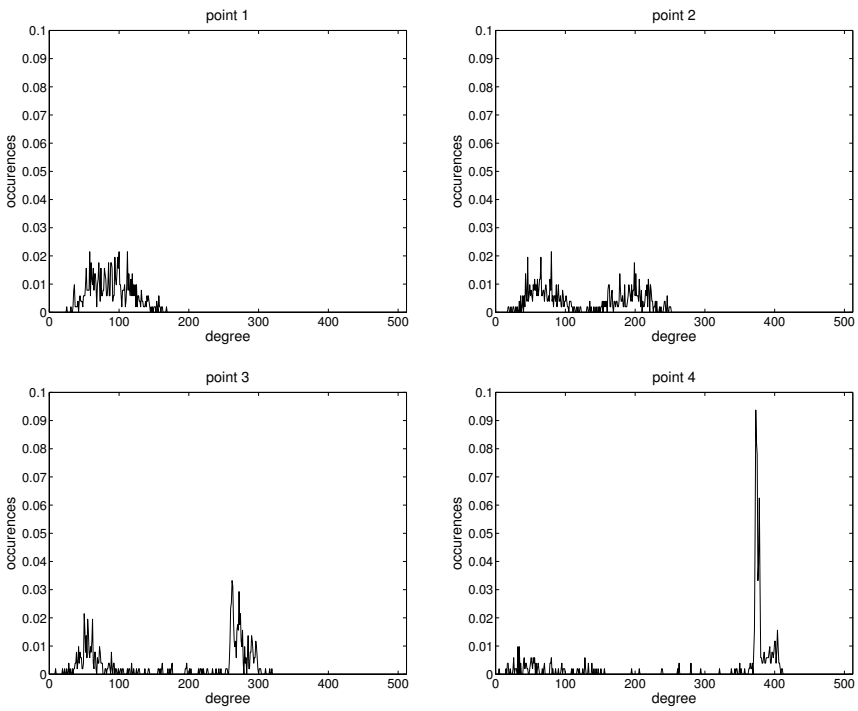

Figure 5.3: Degree distribution of the temperature network at each of the four points approaching the tipping point. On the horizontal axis the degree is shown, on the vertical axis the occurrence of a particular degree.

5.3 Empirical Orthogonal Functions (EOFs)

As in chapter 4, we decompose the data and construct the first three EOFs of the temperature data at each of the four points approaching the tipping point. These three EOFs account for 90% to 97% of the total variability. Figures 5.4 to 5.6 show the evolution of the three EOFs along the bifurcation diagram. Below each figure, it is also shown how the importance of each EOF changes.

As was the case for a symmetrically forced MOC, we see that EOF1 increases in importance when approaching the tipping point. EOF2 and EOF3 on the other hand, decrease in importance.

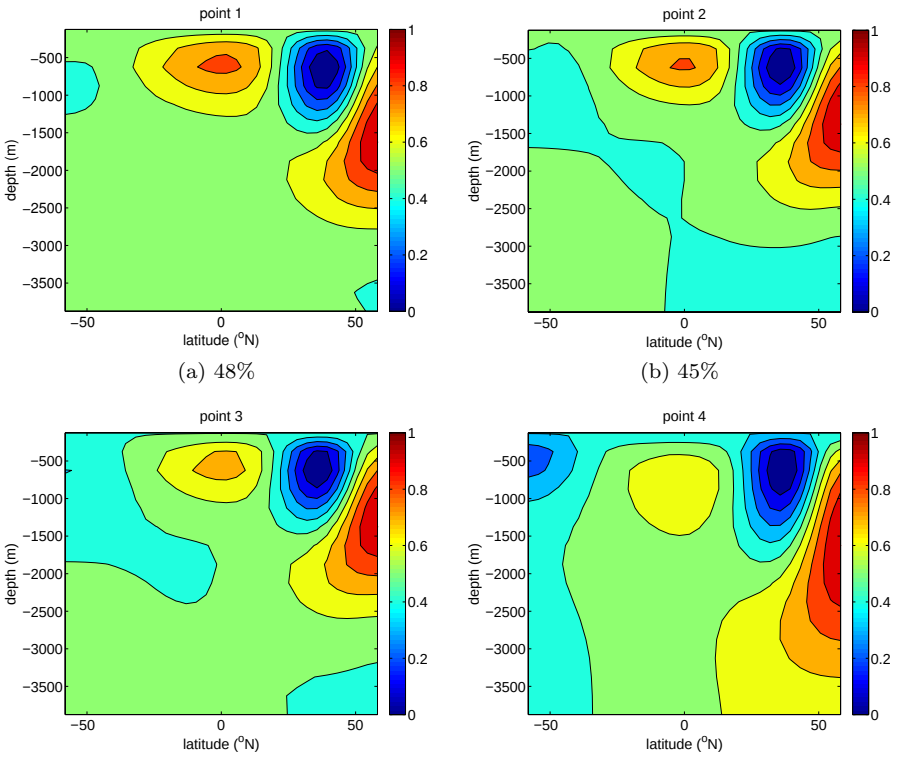

(a) 48% (b) 45%

(c) 41% (d) 77%

Figure 5.4: Pattern of the first EOF of the temperature field at each of the four points approaching the tipping point. The percentage of the variance that is explained by EOF1 is indicated below each figure.

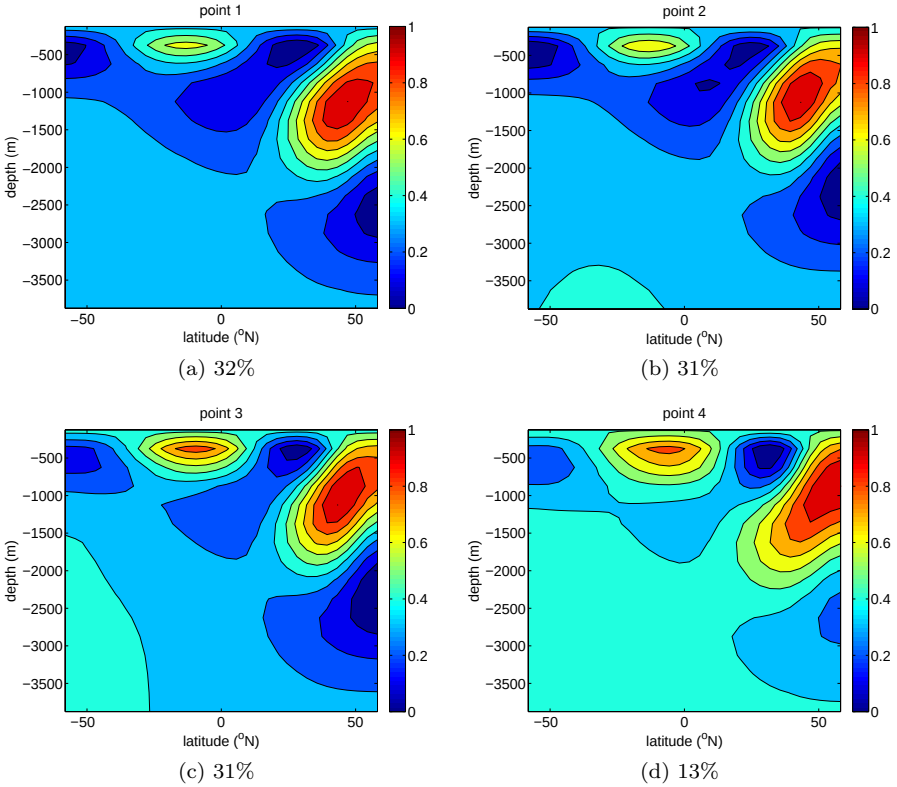

(a) 32% (b) 31%

(c) 31% (d) 13%

Figure 5.5: Pattern of the second EOF of the temperature field at each of the four points approaching the tipping point. The percentage of the variance that is explained by EOF2 is indicated below each figure.

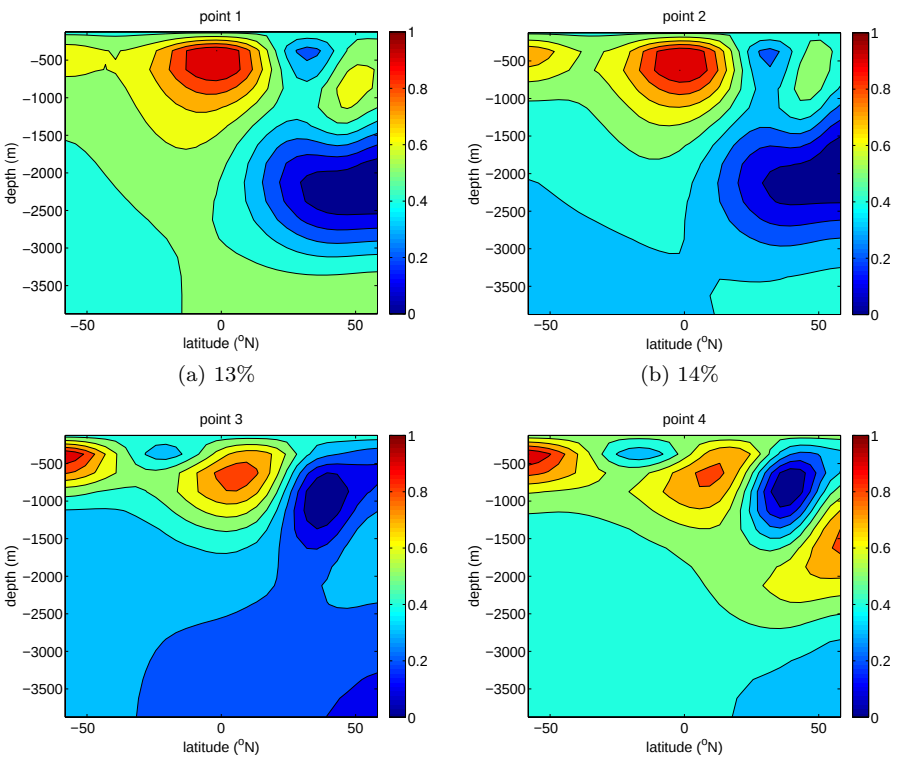

(a) 13% (b) 14%

(c) 18% (d) 7%

Figure 5.6: Pattern of the third EOF of the temperature field at each of the four points approaching the tipping point. The percentage of the variance that is explained by EOF3 is indicated below each figure.

5.3.1 Reconstructed Networks

By once again partly reconstructing the temperature data from the first three EOFs as

$$
\begin{aligned}
F_1 &= \mathbf{a}_1\mathbf{c}_1^T, \\
F_2 &= \mathbf{a}_1\mathbf{c}_1^T + \mathbf{a}_2\mathbf{c}_2^T, \\
F_3 &= \mathbf{a}_1\mathbf{c}_1^T + \mathbf{a}_2\mathbf{c}_2^T + \mathbf{a}_3\mathbf{c}_3^T,
\end{aligned}
$$

we can create networks from F_2 and F_3. These reconstructed temperature networks are shown in figures 5.7 and 5.8.

The degree of both the network constructed from F_2 and from F_3 strongly resembles the degree field of the original network in figure 5.2. For the network constructed from F_2 we see that the degree in general is too high and islands of higher degree appear in the top layer of the basin. The degree is lowered when EOF3 is added in the network constructed from F_3 and the islands also disappear.

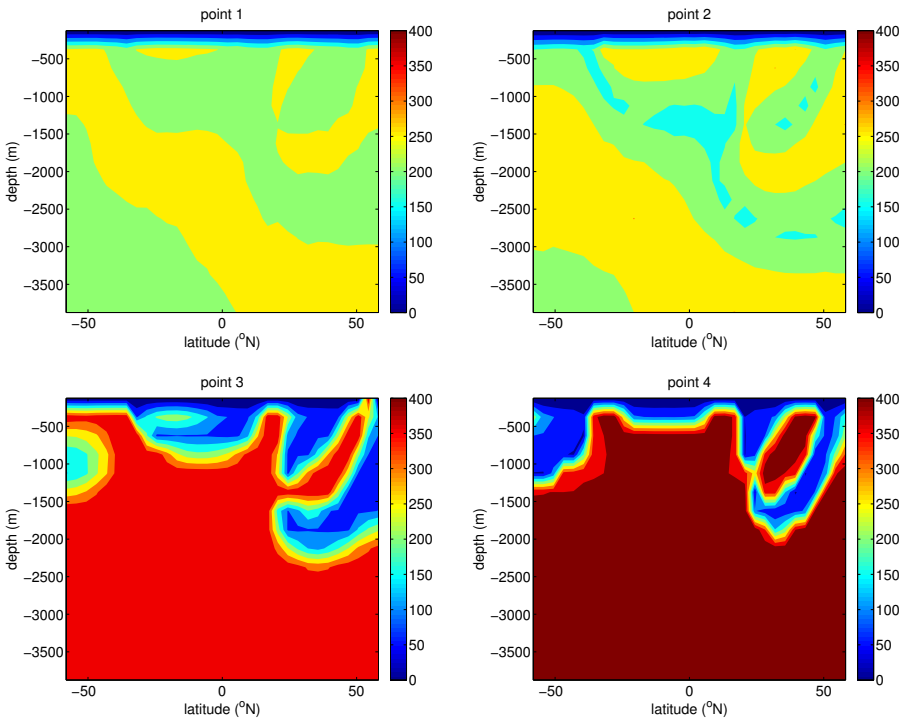

Figure 5.7: Degree of the network constructed from F_2 of the temperature, with threshold value $\tau = 0.7$, shown at each of the four points approaching the tipping point.

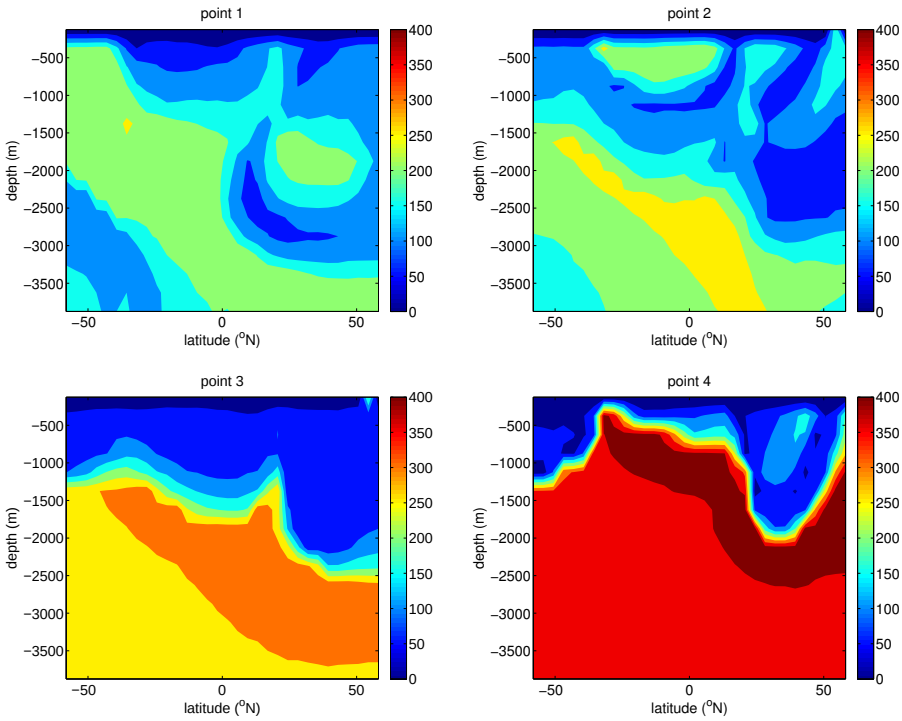

Figure 5.8: Degree of the network constructed from F_3 of the temperature, with threshold value $\tau = 0.7$, shown at each of the four points approaching the tipping point.

5.4 Limited grid networks

We again consider the limited depth-surface and north-south grids of figure 4.25. We construct the temperature networks from these two grids at each of the four points. The degree of the networks is shown in figure 5.9 and 5.10.

In the degree of the depth-surface network we see different behaviour at the surface and at the bottom. The degree at the bottom of the basin (blue) increases when approaching the tipping point, whereas the surface degree (red) does not show any clear evolution. The same effect is seen in the degree of the north-south network.

We can also plot the degree distributions of these networks. This is shown in figures 5.11 and 5.12. As expected, we once again see that there is a separation of two peaks upon approaching the tipping point. The number of nodes with high degree also increases.

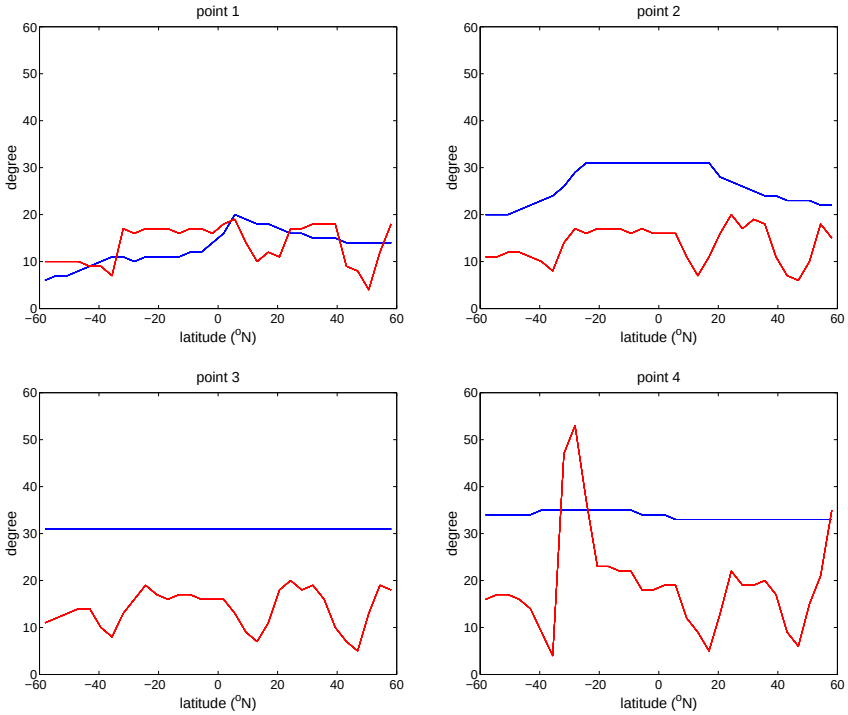

Figure 5.9: Degree of the network constructed from the depth-surface temperature grid. The blue line shows the degree at the bottom of the basin, red the degree at the surface. Latitude is plotted on the horizontal axis, degree on the vertical.

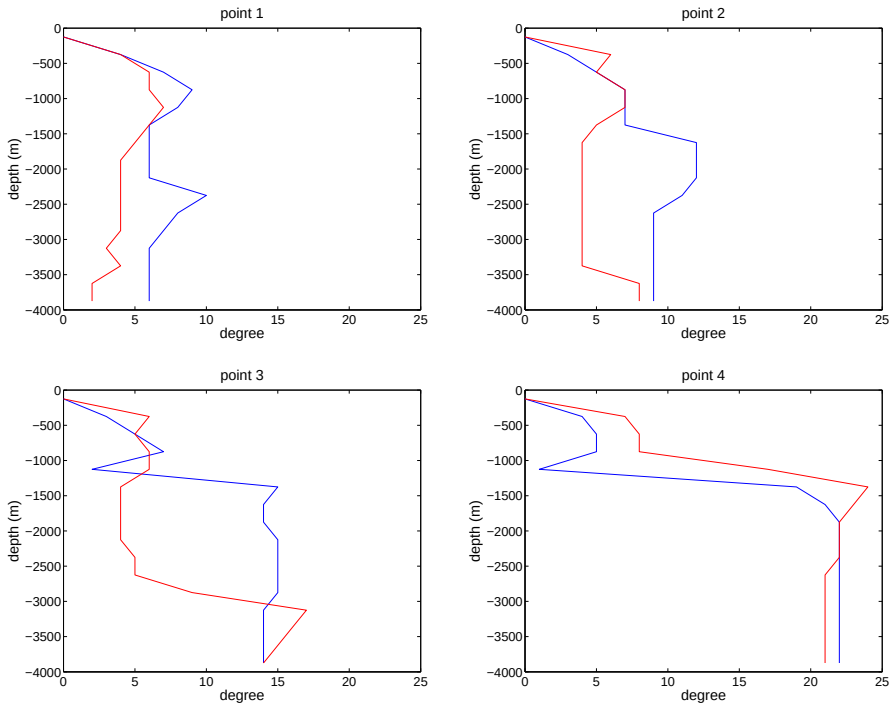

Figure 5.10: Degree of the network constructed from the north-south temperature grid. The blue line shows the degree of the nodes in the south, red the degree of the nodes in the north. Degree is plotted on the horizontal axis, depth on the vertical.

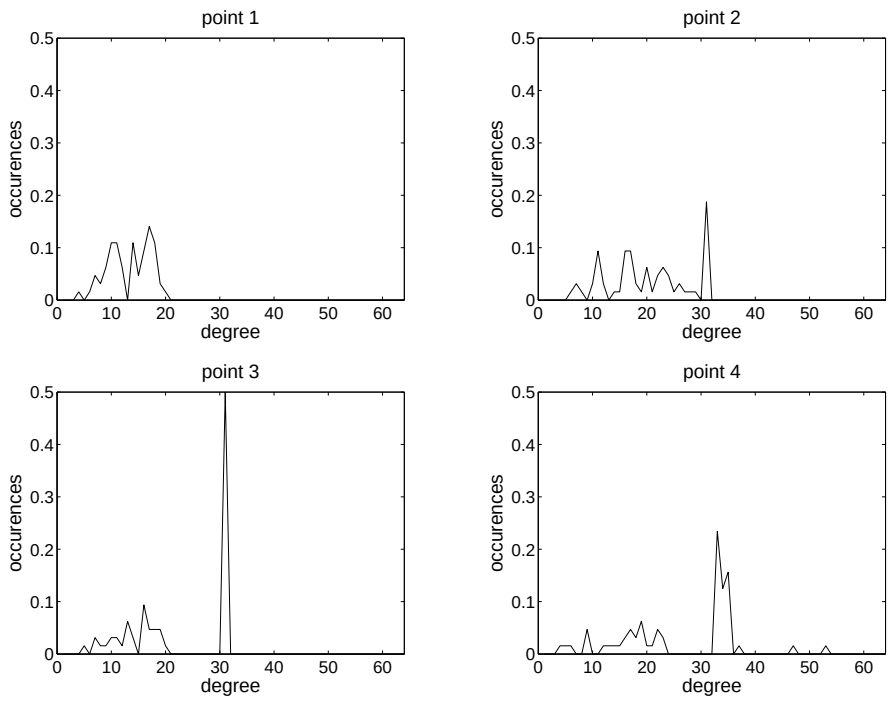

Figure 5.11: Degree distribution of the temperature network in each of the four points approaching the tipping point, constructed from the depth-surface grid.

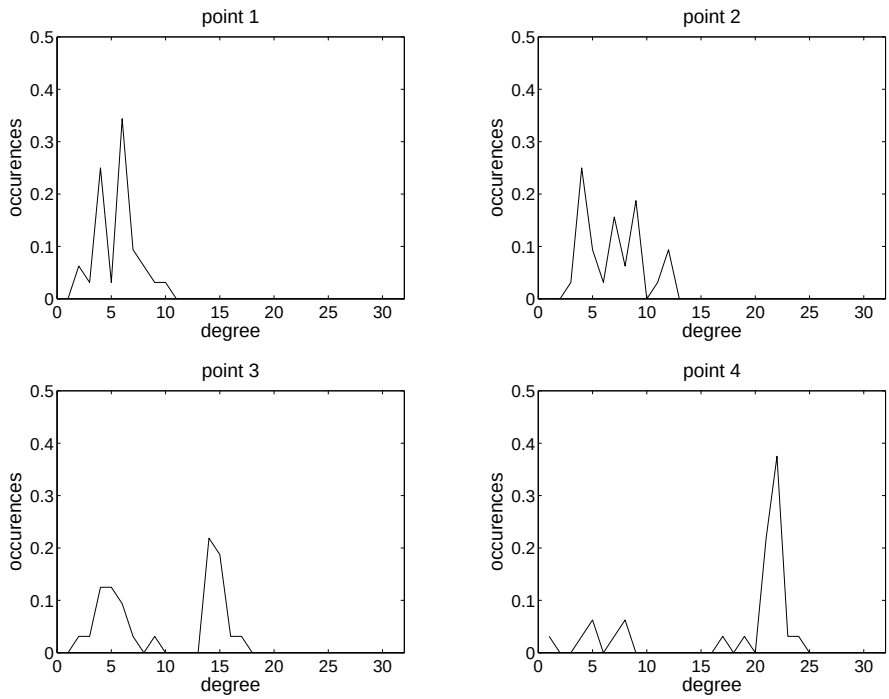

Figure 5.12: Degree distribution of the temperature network in each of the four points approaching the tipping point, constructed from the north-south grid.

5.5 Warning signal

In chapter 4 we saw that in our case, the most useful indicator that can provide an early warning signal was the degree ratio d_r, defined in equation 4.3. Therefore, we also compute the degree ratio of the temperature in case of asymmetrical forcing of the MOC. We calculate d_r in each of the four points indicated in the bifurcation diagram in figure 5.1 and in three extra intermediate points. In figure 5.13 the degree ratio of the networks constructed from the original temperature grid (black), the depth-surface grid (blue) and the north-south grid (red) is plotted against the asymmetrical freshwater flux parameter β_n.

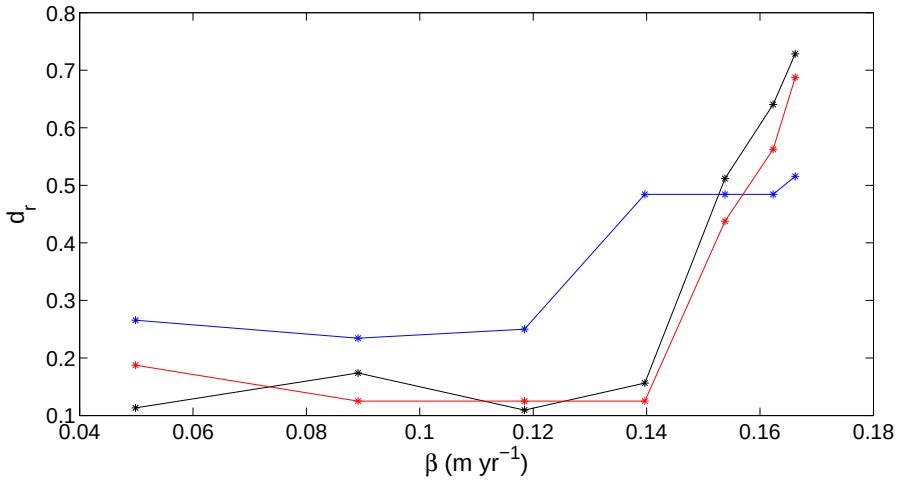

Figure 5.13: Degree ratio as a function of the asymmetrical freshwater parameter β_n, constructed from the original temperature network (black), the network from the depth-surface grid (blue) and from the north-south grid (red).

If we again set a threshold $d_r \geq 0.5$, we see that in case of the temperature, the original network and the network from the north-south grid provide us with an early warning signal. The network constructed from the depth-surface grid does not give a warning. These results are the same as for the symmetrical forcing.

Chapter 6

Discussion and Conclusion

From the results shown in chapters 4 and 5, there was a clear evolution in the temperature and salinity networks when approaching the tipping point of the Atlantic Meridional Overturning Circulation. In both the temperature and salinity networks the degree increased in most -but mainly in the bottom- of the Atlantic basin.

When we considered the eigenvectors of the symmetrically forced system, we saw that they had the same general shape as the network degree. This suggests that these eigenvectors might be the dominant modes of the system but it does not satisfactorily explain the evolution of the network.

The empirical orthogonal functions provided us with more insight. We saw that the first EOFs of the temperature of both the symmetrically and asymmetrically forced MOC explained an increasing amount of the variance when the tipping point was approached. Since the network of the first EOF is fully connected, it follows that the total network also becomes more connected and therefore the degree increases. The second and third temperature EOFs then provide the network with its smaller scale structure and the lower degree at the surface. In case of the salinity EOFs, the first EOF did not increase in importance when approaching the tipping point, the third EOF on the other hand did. We also saw that the third EOF was much more important in the reconstructed salinity networks than was the case for the reconstructed temperature networks. This is explained by the increasing importance of the third salinity EOF.

To test whether the evolution of the networks when approaching the tipping point was still apparent when constructed from fewer nodes, we considered limited grids. For both the symmetrically and asymmetrically forced systems, we constructed networks of the temperature from a depth-surface and north-south grid. In the lower layers, the increasing network degree was still observed.

To find an indicator that can provide an early warning signal of the approaching tipping point, we considered the degree ratio and set a threshold value of $d_r \geq 0.5$. This indicator works well for the temperature networks constructed from the full original grid and from the north-south grid. In case of the depth-surface grid however, no warning was provided. This is probably because the temperature network at the bottom of the basin becomes highly interconnected, but does not form links with the nodes at the surface. Because of this, the degree ratio does not reach above 0.5. By no longer including the nodes at the surface in the grid, this problem will very possibly be resolved. For the symmetrically forced MOC, we also considered the degree ratio of the salinity. The threshold of 0.5 does provide a warning signal, but it is given closer to the tipping point than was the case for the temperature. Since the degree of the salinity network also increases less rapidly than that of the temperature, this was to be expected. To provide an early warning signal from the salinity network, it is better to set the threshold of the degree ratio at a lower value. Using the threshold of the degree ratio as an early warning indicator has the advantage that no records of previous situations are needed. On the other hand, this indicator might be prone to errors and false alarms can be triggered. Therefore, the development of a more advanced indicator is probably desirable.

In conclusion, by constructing temperature and salinity networks in the meridional-depth plane of the Atlantic MOC, we have shown that there is a clear evolution in the network degree when approaching the tipping point of the MOC. The degree ratio increases steeply and can be used as an early warning indicator. The advantages of this indicator with respect to early ones based on temporal correlation, is that shorter time series can be used. The disadvantage is that the indicator is based on a network of spatial measurements. We showed, however, that only with a partial set of grid points, the indicator may

be valuable to warn for the approaching tipping point.

These results should be directly applicable to output from general circulation models. They furthermore show that to apply them to observations, a good spatial resolution in measurements is desirable. With a potential application to determine whether transitions in the MOC have been involved in the Dansgaard-Oeschger events, well synchronised records of ocean bottom temperature are desired.

Appendix A

Network tests

A.1 Networks with different thresholds

We have also constructed networks with different threshold values $\tau = 0.6$ and $\tau = 0.8$. The degrees of these networks for both temperature and salinity are shown in figures A.1 to A.4. Results are not different from the threshold value of $\tau = 0.7$.

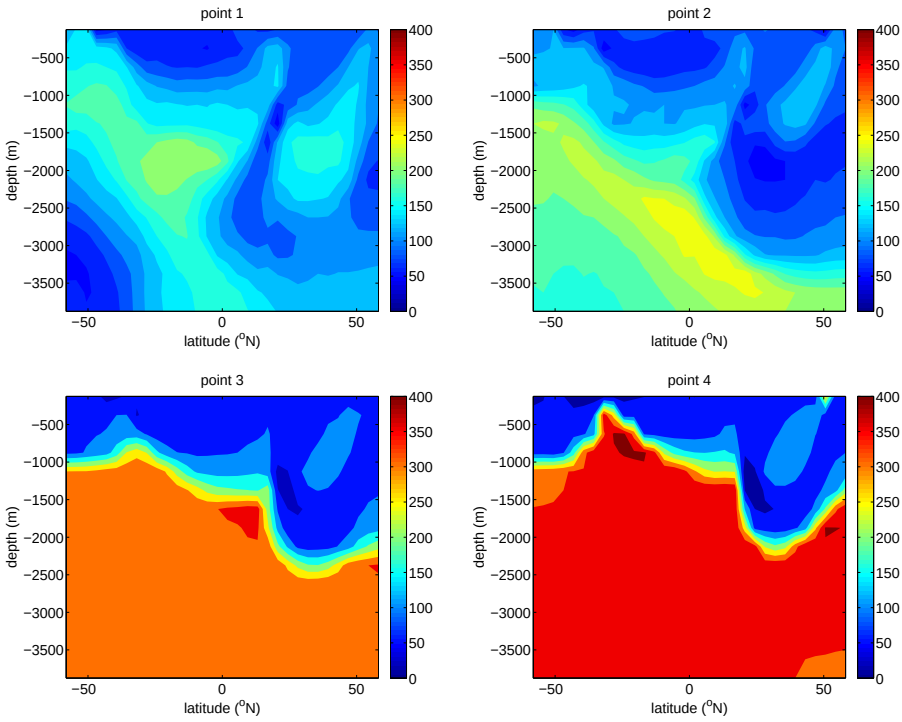

Figure A.1: Network degree of the temperature, constructed with threshold value $\tau = 0.6$.

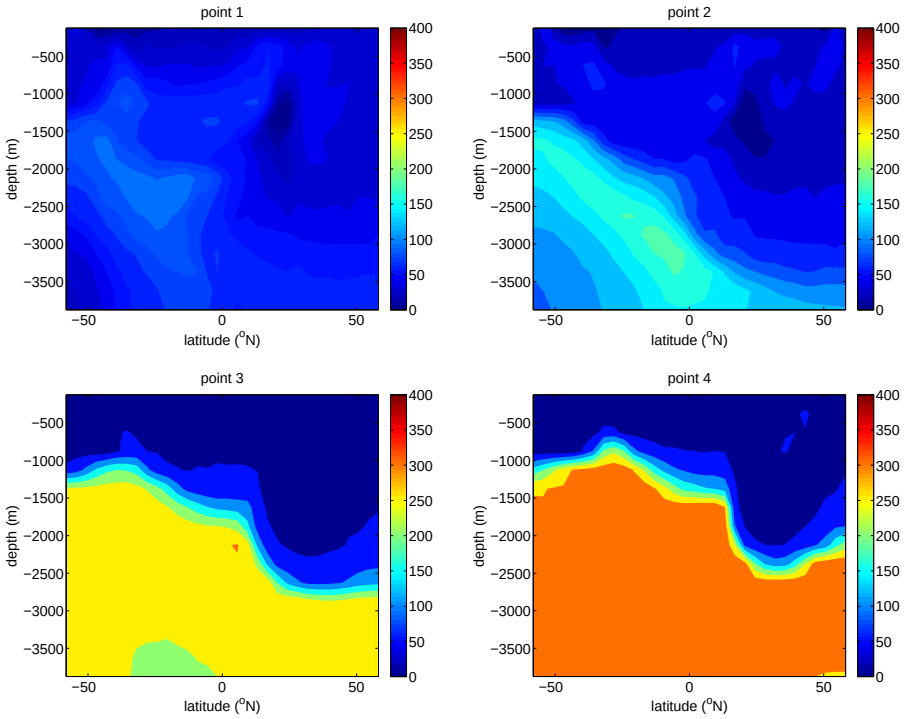

Figure A.2: Network degree of the temperature, constructed with threshold value $\tau = 0.8$.

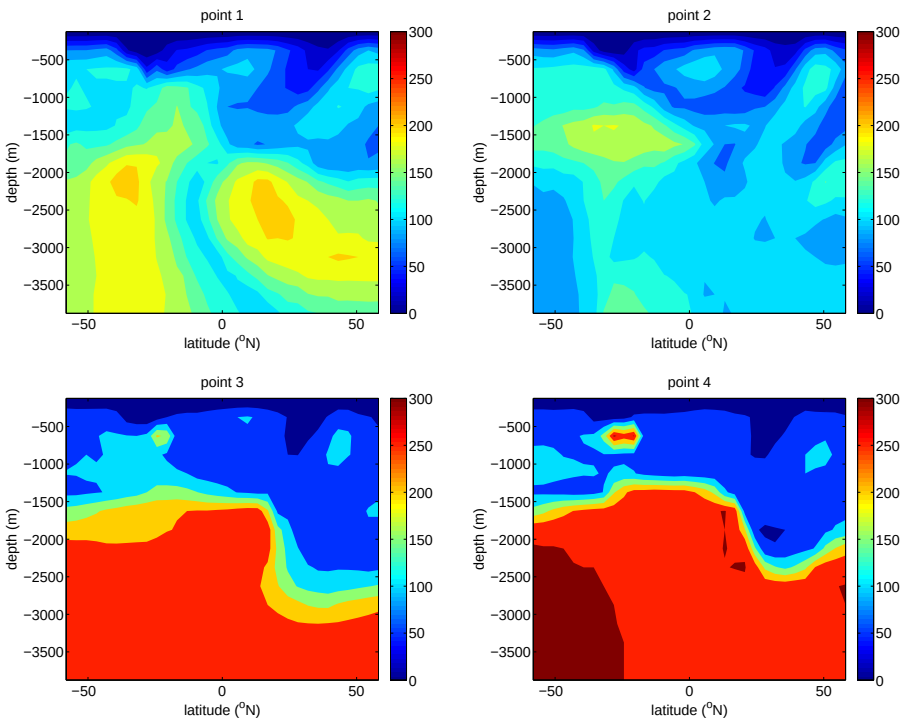

Figure A.3: Network degree of the salinity, constructed with threshold value $\tau = 0.6$.

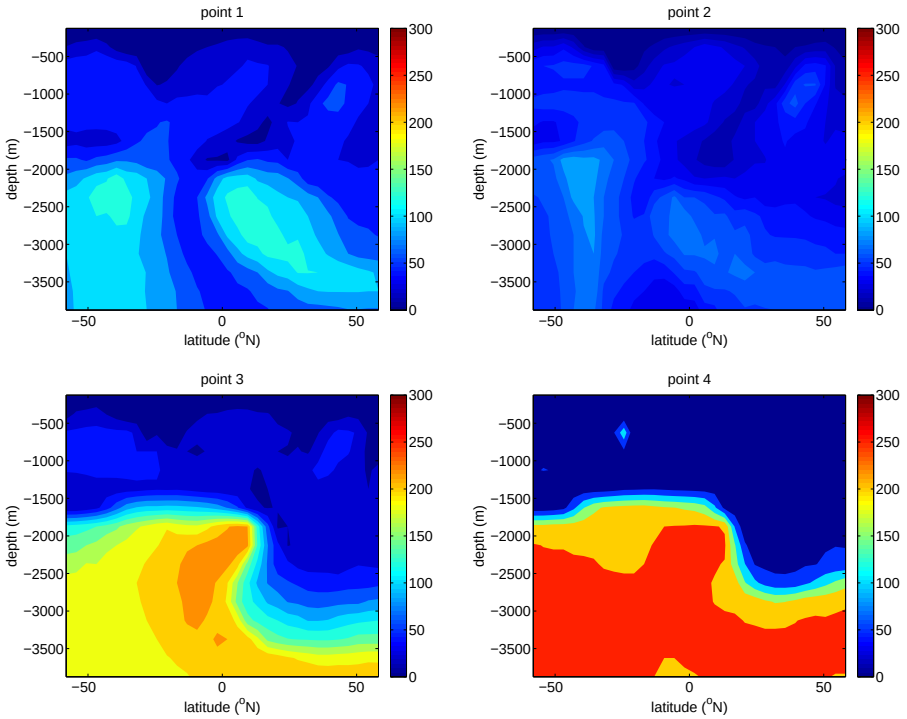

Figure A.4: Network degree of the salinity, constructed with threshold value $\tau = 0.8$.

A.2 Networks from longer time series

We have also constructed networks where THCM was run for a period of 2000 years rather than 500 years. Results are shown in figures A.5 and A.6. The network degree still increases when approaching the tipping point, however the surface area with a low degree decreases.

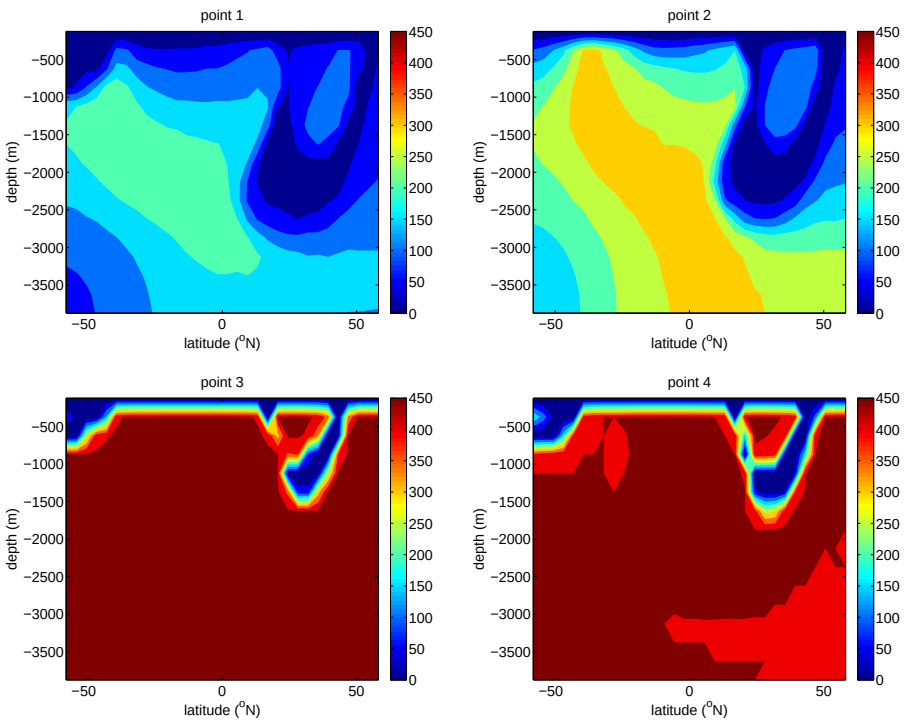

Figure A.5: Network degree of the temperature, constructed from a 2000 year run of THCM. Threshold value $\tau = 0.7$.

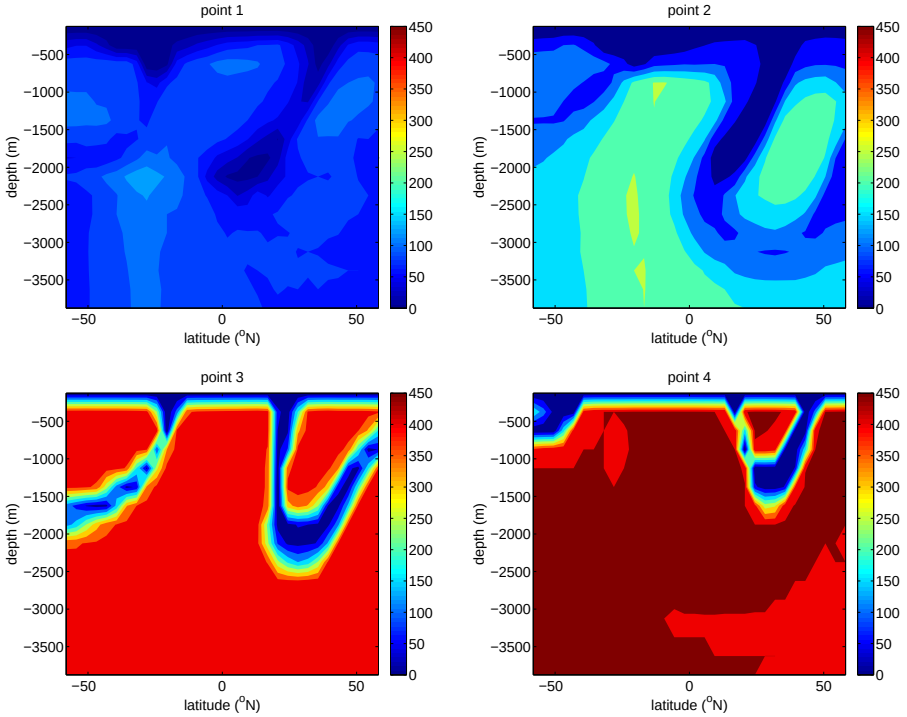

Figure A.6: Network degree of the salinity, constructed from a 2000 year run of THCM. Threshold value $\tau = 0.7$.

Bibliography

Army Service Forces Manual M-101. Ocean currents and sea ice from atlas of world maps, 1943. United States Army Service Forces, Army Specialized Training Division.

G. Bond, W. Broecker, S. Johnsen, J. McManus, L. Labeyrie, J. Jouzel, and G. Bonani. Correlations between climate records from the North Atlantic sediments and Greenland ice. *Nature*, 365:143–147, 1993.

F.O. Bryan. High-latitude salinity effects and interhemispheric thermohaline circulations. *Nature*, 323: 301–304, 1986.

A. Cho. Ourselves and our interactions: the ultimate physics problem? *Science*, 325:406–408, 2009.

A.C. Clement and L.C. Peterson. Mechanisms of abrupt climate change of the last glacial period. *Reviews of Geophysics*, 46:RG4002, 2008.

W. Dansgaard, S.J. Johnsen, H.B. Clausen, D. Dahl-Jensen, N.S. Gundestrup, C.U. Hammer, C.S. Hvidberg, J.P. Steffensen, A.E. Sveinbjornsdottir, J. Jouzel, and G. Bond. Evidence for general instability of past climate from a 250-kyr ice-core record. *Nature*, 364:218–220, 1993.

M. den Toom, H.A. Dijkstra, and F.W. Wubs. Spurious multiple equilibria introduced by convective adjustment. *Ocean Modelling*, 38:126–137, 2011.

H.A. Dijkstra. *Nonlinear physical oceanography: A dynamical systems approach to the large scale ocean circulation and El Niño*, pages 63–119. Springer, second edition, 2005.

H.A. Dijkstra and M. Ghil. Low-frequency variability of the large-scale ocean circulation: a dynamical system approach. *Reviews of Geophysics*, 43:RG3002, 2005.

J. Donges, Y. Zou, N. Marwan, and J. Kurths. Complex networks in climate dynamics. *The European Physical Journal Special Topics*, 174:157–179, 2009.

J. Donges, N. Marwan, and R. Donner, June 2012. http://www.pik-potsdam.de/members/donges/software-1.

R.J. Stouffer et al. Investigating the causes of the response of the thermohaline circulation to past and future climate changes. *Journal of Climate*, 19:1365–1387, 2006.

A. Gozolchiani and S. Havlin. The emergence of El Niño as an autonomous component in the climate network. arXiv:1010.2605v1, 2010.

J.M. Gregory, K.W. Dixon, R.J. Stouffer, A.J. Weaver, E. Driesschaert, M. Eby, T. Fichefet, H. Hasumi, A. Hu, J.H. Jungclaus, I.V. Kamenkovich, A. Levermann, M. Montoya, S. Murakami, S. Nawrath, A. Oka, A.P. Sokolov, and R.B. Thorpe. A model intercomparison of changes in the Atlantic thermohaline circulation in response to increasing atmospheric CO2 concentration. *Geophysical Research Letters*, 32:L12703, 2005.

H. Held and T. Kleinen. Detection of climate system bifurcations by degenerate fingerprinting. *Geophyscial Research Letters*, 31:L23207, 2004.

R. Knutti, J. Fluckiger, T.F. Stocker, and A. Timmerman. Strong hemispheric coupling of glacial climate through freshwater discharge and ocean circulation. *Nature*, 430:851–856, 2004.

C. Kuehn. A mathematical framework for critical transitions: Bifurcations, fast-slow systems and stochastic dynamics. *Physica D-Nonlinear Phenomena*, 240:1020–1035, 2011.

T.M. Lenton and H.J. Schnellnhuber. Tipping the scales. *Nature Reports Climate Change*, 1:97–98, 2007.

V.N. Livina, F. Kwasniok, and T.M. Lenton. Potential analysis reveals changing number of climate states during the last 60 kyr. *Climate of the Past*, 6, 2010.

E. Maier-Reimer and U. Mikolajewicz. Experiments with an ogcm on the cause of the younger dryas, 1989.

G.A. Meehl, T.F. Stocker, W.D. Collins, P. Friedlingstein, A.T. Gaye, J.M. Gregory, A. Kitoh, R. Knutti, J.M. Murphy, A. Noda, S.C.B. Raper, I.G. Watterson, A.J. Weaver, and Z.C. Zhao. Global climate projections. In *Climate Change 2007: The Physical Science Basis. Contribution of Working Group I to the Fourth Assessment Report of the Intergovernmental Panel on Climate Change [Solomon, S., D. Qin, M. Manning, Z. Chen, M. Marquis, K.B. Averyt, M. Tignor and H.L. Miller (eds.)]*. 2007.

J.M. Mitchell. An overview of climate variability and its causal mechanisms. *Quarternary Research*, 6: 481–493, 1976.

S. Rhamstorf. Bifurcations of the Atlantic thermohaline circulation in response to changes in the hydrological cycle. *Nature*, 378:145–149, 1995.

H.E. Stanley and S. Havlin. Social networks: from sexual networks to threatened networks. In *Statistical mechanics of complex networks*, volume 625 of *Lecture notes in physics*, pages 167–174. Springer Berlin / Heidelberg, 2003.

K. Steinhaeuser, N.V. Chawla, and A.R. Ganguly. Complex networks in climate science: progress, opportunities and challenges, 2010. Conference on intelligent data understanding.

H. Stommel. Thermohaline convection with two stable regimes of flow. *Tellus*, 2:224–230, 1961.

S.H. Strogatz. *Nonlinear dynamics and chaos: With applications to physics, biology, chemistry and engineering*. Perseus Books, 1994.

O. Thual and J.C. McWilliams. The catastrophe structure of thermohaline convection in a two-dimensional fluid model and a comparison with low-order box models. *Geophysical and Astrophysical fluiddynamics*, 64:67–95, 1992.

A.A. Tsonis and P.J. Roebber. The architecture of the climate network. *Physica A: Statistical Mechanics and its Applications*, 333:497–504, 2004.

A.A. Tsonis, K.L. Swanson, and G. Wang. On the role of atmospheric teleconnections in climate. *Journal of Climate*, 21:2990–3001, 2008.

M. Vellinga and R.A. Wood. Global climatic impacts of a collapse of the atlantic thermohaline circulation. *Climatic Change*, 54:251–267, 2002.

K. Yamasaki, A. Gozolchiani, and S. Havlin. Climate networks around the globe are significantly affected by El Niño. *Physical Review Letters*, 100:228501–1–228501–4, 2008.